

**The Centers of Early-Type Galaxies with HST. VI. Bimodal Central Surface
Brightness Profiles.** ¹

Tod R. Lauer

National Optical Astronomy Observatory², P.O. Box 26732, Tucson, AZ 85726

Karl Gebhardt

Department of Astronomy, University of Texas, Austin, Texas 78712

S. M. Faber

*UCO/Lick Observatory, Board of Studies in Astronomy and Astrophysics, University of
California, Santa Cruz, California 95064*

Douglas Richstone

Department of Astronomy, University of Michigan, Ann Arbor, MI 48109

Scott Tremaine

Princeton University Observatory, Peyton Hall, Princeton, NJ 08544

John Kormendy

Department of Astronomy, University of Texas, Austin, Texas 78712

M. C. Aller

Department of Astronomy, University of Michigan, Ann Arbor, MI 48109

Ralf Bender

Universitäts-Sternwarte, Scheinerstraße 1, München 81679, Germany

Alan Dressler

*The Observatories of the Carnegie Institution of Washington, 813 Santa Barbara St., Pasadena,
CA 91101*

Alexei V. Filippenko

Department of Astronomy, University of California, Berkeley, CA 94720-3411

Richard Green

LBT Observatory, University of Arizona, Tucson, AZ 85721

Luis C. Ho

*The Observatories of the Carnegie Institution of Washington, 813 Santa Barbara St., Pasadena,
CA 91101*

ABSTRACT

We combine the results from several *HST* investigations of the central structure of early-type galaxies to generate a large sample of parameterized surface photometry. The studies selected for inclusion were those that used the “Nuker law” to characterize the inner light distributions of the galaxies. The sample comprises WFPC1 and WFPC2 *V* band observations published earlier by our group, *R* band WFPC2 photometry of Rest et al., NICMOS *H* band photometry by Ravindranath et al. and Quillen et al., and the brightest cluster galaxy WFPC2 *I* band photometry of Laine et al. All parameters are transformed to the *V* band and a common distance scale. The distribution of the logarithmic slopes of the central brightness profiles strongly affirms that the central structure of elliptical galaxies with $M_V < -19$ is bimodal, based on both parametric and non-parametric analysis. At the *HST* resolution limit, most galaxies are either power-law systems, which have steep cusps in surface brightness, or core systems, which have shallow cusps interior to a steeper envelope brightness distribution. A rapid transition between the two forms occurs over the luminosity range $-22 < M_V < -20$, with cores dominating at the highest luminosities, and power-laws at the lowest. There are a few “intermediate” systems that have both cusp slopes and total luminosities that fall within the core/power-law transition, but they are rare and do not fill in the overall bimodal distribution of cusp slopes. These results are inconsistent with the Ferrarese et al. Virgo Cluster Survey (VCS) analysis, which did not find a bimodal distribution of cusp slopes. While the VCS ACS/WFC images have lower angular resolution than the WFPC2/PC F555W images used for much of the sample, the basic galaxy profiles measured with either camera agree well after deconvolution. However, using galaxies common to the present and VCS samples, we demonstrate that the VCS models of the cusps are either a poor match to the observations or consist of forms fitted to the galaxy envelopes and extrapolated inward to the *HST* resolution limit.

Subject headings: galaxies: nuclei — galaxies: photometry — galaxies: structure

¹Based on observations made with the NASA/ESA *Hubble Space Telescope*, obtained at the Space Telescope Science Institute, which is operated by the Association of Universities for Research in Astronomy, Inc., under NASA contract NAS 5-26555. These observations are associated with GO and GTO proposals # 5236, 5446, 5454, 5512, 5943, 5990, 5999, 6099, 6386, 6554, 6587, 6633, 7468, 8683, and 9107.

²The National Optical Astronomy Observatory is operated by AURA, Inc., under cooperative agreement with the National Science Foundation.

1. Introduction

Long before massive black holes were accepted to be present in the centers of galaxies, Begelman et al. (1980) argued that a binary black hole created in the merger of two galaxies would eject stars from the center of the newly created system as the binary slowly hardened. N-body simulations support this hypothesis (Ebisuzaki et al. 1991; Makino 1997; Milosavljević & Merritt 2001). We now believe that nearly every elliptical galaxy or spiral bulge has a black hole at its center (Magorrian et al. 1998). We also believe that the most massive elliptical galaxies were formed by merging pre-existing galaxies. It is possible that their central structure still bears witness to such events. The “cores” seen at the centers of the most luminous elliptical galaxies may indeed be the signatures of gravitational stirring and heating (“core scouring”) by binary black holes (Faber et al. 1997).

Cores were initially seen in ground-based observations of nearby luminous elliptical galaxies as a central region of nearly constant surface brightness (Lauer 1985; Kormendy 1985). The cores were seen to be non-isothermal, but their true form as $r \rightarrow 0$ was unknown. *HST* images, however, later showed that nearly all galaxies have singular starlight distributions in the sense that surface brightness diverges as $\Sigma(r) \sim r^{-\gamma}$ (Lauer et al. 1991, 1992a,b; Crane et al. 1993; Kormendy et al. 1994; Ferrarese et al. 1994; Lauer et al. 1995). Typically, in low luminosity early-type galaxies, γ decreases only slowly as the center is approached and a steep $\gamma > 0.5$ cusp continues into the *HST* resolution limit; Lauer et al. (1995) classified these systems as “power-law” galaxies. In more luminous galaxies, however, the steep envelope profile transitions to a shallow inner cusp with $\gamma < 0.3$ at a “break radius,” r_b . This behavior was seen in galaxies that had cores from ground-based observations; the break radius roughly corresponded to what had been measured as the core radius. We thus chose to continue to call these “core galaxies,” even though the shallow cusps in projected brightness in most³ of these systems imply steep and singular cusps in luminosity density (Lauer et al. 1995).

A strong justification of this classification schema was that the distribution of γ' over a sample of early-type galaxies was seen to be strongly bimodal (Faber et al. 1997), where γ' is the local cusp slope at the *HST* resolution limit. Initially no galaxies were seen to have $0.3 < \gamma' < 0.5$. It was thus sensible to apply the separate core and power-law classifications to the two distinct and cleanly separated peaks in the γ' distribution. The bimodal distribution was initially inferred from fits to the surface photometry using the “Nuker law” (Lauer et al. 1995; see equation 2), which has the asymptotic form $\Sigma(r) \sim r^{-\gamma}$, as $r \rightarrow 0$, however, Gebhardt et al. (1996) demonstrated that non-parametric treatment of the surface photometry recovered an identical bimodal distribution, and further that bimodality was a feature of the luminosity *density* distributions of early type galaxies, not just the surface brightness distributions.

The core and power-law classifications are fundamental because they correlate with global

³Lauer et al. (2002) and Lauer et al. (2005) identified a number of galaxies in which the brightness profiles actually decreased as $r \rightarrow 0$. These systems thus have $\gamma < 0$ at small radii and do not have cusps in space density.

physical properties that are diagnostic of galaxy formation. Core galaxies are on average more luminous than power-law galaxies, with power-laws dominating below $M_V \sim -21$ and cores greatly dominating at higher luminosities (Faber et al. 1997). Core galaxies generally have boxy isophotes, while power-law galaxies are disk-like (Nieto et al. 1991; Kormendy & Bender 1996; Faber et al. 1997). Core galaxies rotate slowly, while power-law galaxies rotate more rapidly (Faber et al. 1997); similarly, boxy galaxies include slow rotators while disk-like galaxies rotate rapidly (Bender 1988; Bender et al. 1989, 1994; Kormendy & Bender 1996). Core-boxy galaxies show minor-axis rotation indicative of triaxiality, while coreless-disk-like galaxies do not (Kormendy & Bender 1996). And core galaxies are systematically rounder than power-law galaxies (Jaffe et al. 1994; Ferrarese et al. 1994; Ryden et al. 2001; Lauer et al. 2005), just as bright (boxy) galaxies are systematically rounder than faint (disk-like) galaxies (Tremblay & Merritt 1996). Significantly, core and power-law galaxies of identical luminosity can still be separated by all of these secondary characteristics (Faber et al. 1997). Thus central and global properties together point to differences in the formation of core and power-law ellipticals. Kormendy & Bender (1996) propose a revision of the Hubble sequence for elliptical galaxies that recognizes this physical dichotomy, using isophote shape as a convenient surrogate for the above physical properties. More recent work continues to show that power-law and core galaxies have physically distinct properties. Cores (Capetti & Balmaverde 2005; Balmaverde & Capetti 2006), like boxy isophotes (Bender et al. 1989), correlate with radio-loud active nuclei. And cores (Pellegrini 2005), like boxy isophotes (Bender et al. 1989), correlate with strong x-ray emission.

The properties of the power-law versus core galaxies suggest that core systems resulted from the mergers of less luminous power-law systems. Simulations by Milosavljević & Merritt (2001), for example, showed that the merger of two power-law galaxies, each with a central massive black hole, would produce a core galaxy. The bimodal cusp distribution would thus be one key to understanding the central structure of elliptical galaxies over a history of mergers.

As larger samples of elliptical galaxies were observed with *HST*, the bimodal slope distribution remained robust (Quillen et al. 2000; Rest et al. 2001; Ravindranath et al. 2001; Lauer et al. 2005). While all of these studies identified a small number of “intermediate” galaxies, which have limiting cusp slopes with $0.3 < \gamma' < 0.5$, they are not common enough to fill the “valley” between the power-law and core cusp-slope distributions. This is a critical point that has often been misunderstood in the literature. The sample of galaxies available to Faber et al. (1997) had no systems with $0.3 < \gamma' < 0.5$, thus the distributions of slopes was not only bimodal, but disjoint. The subsequent discovery of a small number of intermediate galaxies shows that the distribution of cusp slopes is truly continuous, but it has remained bimodal in its overall character in all the studies cited above.

This picture has been challenged by the recent distribution of cusp slopes presented by Ferrarese et al. (2006), who do not find bimodality in their sample of 100 galaxies observed by their *HST* Virgo Cluster Survey (VCS), although they still identify a separate class of core galaxies, which they define as having brightness profiles that fall below Sérsic (1968) forms in the center. While the use of Sérsic profiles is a new approach to identifying core galaxies, the class of VCS core galaxies

identified in this way is essentially consistent with the definition of core galaxies in earlier studies. The distribution of slopes for the non-core galaxies in Ferrarese et al. (2006), however, does not match that of the power-law galaxies presented in all the studies cited above, even though this set includes several galaxies previously classified as power-laws. The difference between the VCS work and all earlier studies lies not in whether or not there are two classes of galaxies, core and "non-core", but in the form of the central structure of the non-core class. Resolving the different pictures presented by Faber et al. (1997) and the VCS results is crucial to understanding how the central structure of elliptical galaxies varies with luminosity, and how it may change over mergers.

This paper has three goals. We first construct a large sample of galaxies that have had their surface brightness distributions characterized by Nuker law fits. These are reduced to a common photometric and distance scale. This sample provides the basic material for an updated investigation into the relationships between the central structure of galaxies and their more global properties, as was presented in Faber et al. (1997); this new analysis is presented in Lauer et al. (2007). The second goal is to reinvestigate the distribution of cusp slopes in early type galaxies. We find that the distribution of slopes remains strongly bimodal, a conclusion that we ratify with a repeat of the non-parametric analysis presented by Gebhardt et al. (1996). The final task is to bolster this conclusion with a comparison of the analysis of *HST* imagery by Lauer et al. (1995, 2005) to that of Ferrarese et al. (2006). We show that the VCS surface photometry models do not accurately recover the distribution of γ' for galaxies with $M_V < -19$.

2. Compilation of a Large Sample of Early-Type Galaxy Central Structure

We define a combined sample of 219 early-type galaxies observed with *HST* for which Nuker-law parameters have been derived by a variety of studies (Lauer et al. 1995; Faber et al. 1997; Quillen et al. 2000; Rest et al. 2001; Ravindranath et al. 2001; Laine et al. 2002; Lauer et al. 2005). The global properties of the sample galaxies are listed in Table 1. The Nuker law parameterizations of the central structure of the galaxies are listed in Table 2.

The investigations cited above were generally done in different photometric bands, and used a variety of sources for galaxy distances, luminosities, and so on. We have adopted the F555W or *V* band as the common photometric system, which was the choice of Lauer et al. (1995), Faber et al. (1997), and Lauer et al. (2005). We also specify the absolute galaxy luminosities in the *V* band. Luminosities are based on the V_T apparent magnitudes published in the RC3 (de Vaucouleurs et al. 1991), with the exception of a few galaxies that had to be transformed from B_T , and the Laine et al. (2002) BGC sample, which provided total magnitudes in the *R* band. Morphologies are also provided by the RC3. Many of the galaxies in the sample are S0 systems rather than true ellipticals. As bulge parameters, rather than those of the whole galaxy, are relevant to the properties of central black holes (Magorrian et al. 1998; Gebhardt et al. 2000; Kormendy & Gebhardt 2001), we have corrected (when possible) the total luminosities of the S0 galaxies for their disk components. Most of the corrections were based on the bulge-disk decompositions of Baggett et al. (1998); other

decompositions were provided by Kormendy & Illingworth (1983), Simien & de Vaucouleurs (1986), Kent (1985), Boroson (1981), and Burstein (1979). When a galaxy appeared in multiple sources we selected the median disk correction. The final disk corrections and sources are given in Table 1.

Calculation of absolute magnitudes is complicated by the heterogeneous quality of distance information across the sample. We set the overall scale to $H_0 = 70 \text{ km s}^{-1} \text{ Mpc}^{-1}$ and have reworked the distances in all references. Our preferred source of distances is the Tonry et al. (2001) surface brightness fluctuation (SBF) survey, but using the group memberships in Faber et al. (1989) and averaging the SBF distances over the group. As the Tonry et al. (2001) SBF scale is consistent with $H_0 = 74$, however, we scale up their SBF distances by 6%. For galaxies not in the SBF catalogue but that are in the Faber et al. (1997) sample, we rescale the distances in that paper from its scale of $H_0 = 80$. For galaxies not in either sample, we check for possible membership in the Faber et al. (1989) group catalogues, using the group velocity in the cosmic microwave background (CMB) frame, if a group SBF distance is not available. Lastly, if no group information is available, we use the galaxy’s velocity in the CMB frame. The distances adopted are given in Table 1; the distance references listed correspond to the four choices, in order of priority, that we have listed here. Absolute luminosities were calculated using the Schlegel et al. (1998) Galactic extinction values.

Table 1 also lists the major-axis effective radii of the galaxies. Effective radii were determined by fitting $r^{1/4}$ -laws to ground-based surface photometry profiles available in the published literature (Lauer et al; in preparation); unfortunately, supporting ground-based surface photometry could not be located for 30% of the sample. No attempt was made to fit S0 galaxies with separate bulge and disk components, so the effective radii may be suspect when the disk contributes significantly to the total galaxy luminosity. Under these general guidelines, we discuss the specific details and treatment applied to each data source for the sample. The samples are given in order of preference, as will be explained in §2.7

2.1. The Lauer et al. (2005) WFPC2 Sample

Lauer et al. (2005) present images and surface photometry for 77 early-type galaxies observed with *HST*+WFPC2, with the galaxies centered in the high-resolution PC1 CCD; 55 of these were obtained under programs GO 5512, 6099, 6587, and 9107, which were carried out by our collaboration. Lauer et al. (2005) also include an independent reduction of the galaxies observed in GO 5454 (Carollo et al. 1997). There is no single criterion that characterizes this combined sample. In general, it comprises relatively luminous nearby elliptical and early-S0 galaxies that could be investigated spectroscopically with *HST* to detect and “weigh” nuclear black holes. The selection of galaxies was heavily influenced by the central-structure parameter relationships presented by Faber et al. (1997). Several galaxies were chosen to sample the luminosity range over which power-law and core galaxies coexist, to explore the transition between the two types. Others were selected to extend the luminosity range of the core parameter relationships. Overall, the sample is rich in

core galaxies, with relatively few power-law galaxies; thus it is complementary to the Rest et al. (2001) sample, which is rich in power-law galaxies. The adopted resolution limit, which is the scale at which γ' is evaluated, is $r_0 = 0''.04$ for most galaxies, but $r_0 = 0''.02$ for some systems for which double-sampled images were available.

2.2. The Rest et al. (2001) WFPC2 Sample

Rest et al. (2001) observed 68 early-type galaxies in the F702W filter with WFPC2 PC1. Their sample comprises early-type galaxies within 3400 km s^{-1} , $M_V < -18.5$, and Galactic latitude $> 20^\circ$. Rest et al. measured surface photometry from deconvolved images and fitted Nuker laws to the profiles. We adopted the parameters in Rest et al., using $F702W - F555W = 0.61$ to transform the surface photometry. One caveat is that Rest et al. adopted $r_0 = 0''.1$ as the resolution limit of their profiles, using the cusp slope at this radius for profile classification. We consider this resolution limit to be unduly conservative for deconvolved WFPC2 images, and thus used their Nuker fits at $r_0 = 0''.04$ instead to determine γ' . As a result, all “intermediate” galaxies in Rest et al. are considered here to have resolved cores, while a number of their power-law galaxies are now classified as intermediates (see the note column in Table 2).

2.3. The Laine et al. (2002) WFPC2 BCG Sample

Laine et al. (2002) obtained WFPC2 PC1 images of 81 brightest cluster galaxies (BCGs) in the F814W filter. The BCG sample was drawn from the volume-limited BCG sample of Postman & Lauer (1995). The photometry was derived from deconvolved images; the Nuker law parameters are combined into the sample, using $V - I = 1.4$ to transform the F814W photometry to F555W, and $V - R = 0.5$ to transform the R total galaxy apparent magnitudes listed in Laine et al. (2002). BCG distances were based on the CMB-frame cluster velocities tabulated by Postman & Lauer (1995).

2.4. The Lauer et al. (1995) and Faber et al. (1997) WFPC1 Sample

The core parameter relationships presented in Faber et al. (1997) were largely based on the Lauer et al. (1995) photometry, but supplemented with a small set of otherwise unpublished WFPC1 GTO galaxies observed and reduced in parallel with the Lauer et al. (1995) galaxies. The Lauer et al. (1995) sample was observed with the F555W filter in the high-resolution PC6 CCD of WFPC1. The surface photometry was measured from deconvolved images; as discussed in Lauer et al. (2005), the profiles should be reliable into $r_0 \approx 0''.1$. Byun et al. (1996) published Nuker-law fits for all the Faber et al. (1997) galaxies. However, we have re-fitted the photometry for this paper to allow for $\gamma < 0$, and in some cases have restricted the radial range of the fits to better isolate the break

radius and inner cusp. The new parameters are also referenced to the major-axis of the galaxies rather than to their mean-radii as was done in Byun et al. (1996).

2.5. The Quillen et al. (2000) NICMOS Sample

Quillen et al. (2000) observed 27 early-type galaxies in the H band with NICMOS2; the sample was largely based on bright nearby elliptical galaxies. Quillen et al. deconvolved their photometry and fitted Nuker laws to the profiles. We have transformed the Quillen et al. photometry using $V - H = 2.95$. We consider the limiting resolution of the NICMOS sample to be $r_0 = 0''.1$.

2.6. The Ravindranath et al. (2001) NICMOS Sample

Ravindranath et al. (2001) presented H band photometry of 33 early-type galaxies based on archival NICMOS2 and NICMOS3 images, many of which were also included in the Quillen et al. (2000) sample. The sample selection in part required galaxy apparent magnitude $B_T < 12.5$ and a northern declination. Ravindranath et al. did not deconvolve their images but chose instead to fit PSF-convolved Nuker laws directly to the images; they also included a central point-source in their fits. We have transformed the Ravindranath et al. photometry to F555W using $V - H = 2.95$ and $B - V = 0.95$ for galaxy apparent magnitudes. Again we use $r_0 = 0''.1$ as the limiting resolution of this sample.

2.7. Galaxies That Appear in Multiple Sources

There is significant overlap between the six sources that contribute to the sample. Given the somewhat heterogeneous nature of the source material and reduction techniques, we have chosen to rank the sources in a preferred order, rather than to average or otherwise blend the parameters for any galaxy observed in more than one sample. Our first preference is for the observations presented by Lauer et al. (2005); as these were derived from F555W WFPC2 images, they have the best spatial resolution of the six studies used. Our next preferences are for the the Rest et al. (2001) F702W profiles, and then the Laine et al. (2002) F814W profiles, as they have successively lower resolution, given the redder filters. While WFPC2 offers superior resolution to WFPC1, deconvolved WFPC1 imagery should still be superior to NICMOS observations made in the near-IR, so the galaxies in Lauer et al. (1995) or Faber et al. (1997) that have no WFPC2 imagery are then next in order of preference. Of the two NICMOS programs, we prefer photometry from Quillen et al. (2000) as they fitted photometry from the deconvolved images directly, rather than fitting PSF-convolved models, which are more vulnerable to systematic errors. The NICMOS programs also provided surface brightness parameters for a number of galaxies that were observed by WFPC2, but that had centers so strongly affected by dust absorption that accurate Nuker law parameters could not

be measured in optical filters.

3. The Bimodality of Central Structure and its Classification

3.1. Core and Power-Law Galaxies

As in our previous analyses of the central structure of early-type galaxies (Kormendy et al. 1994; Lauer et al. 1995; Faber et al. 1997), we classify the systems into two types, core and power-law galaxies, based on the logarithmic slopes, γ' , of their central cusps at the *HST* angular resolution limit, where

$$\gamma'(r_0) \equiv - \left. \frac{d \log I}{d \log r} \right|_{r=r_0}, \quad (1)$$

and r_0 is the *HST* resolution scale or any other limiting radius. In the analysis that follows, we represent $I(r)$ with the “Nuker law” (Lauer et al. 1995) parametric form

$$I(r) = 2^{(\beta-\gamma)/\alpha} I_b \left(\frac{r_b}{r} \right)^\gamma \left[1 + \left(\frac{r}{r_b} \right)^\alpha \right]^{(\gamma-\beta)/\alpha}, \quad (2)$$

which describes the profiles as a “broken power law;” it is an extension of a broken power-law form first used to describe the brightness profile of M32 (Lauer et al. 1992b). Note that γ is the inner cusp slope as $r \rightarrow 0$ and is distinguished from γ' , which is the purely local slope evaluated at the resolution limit noted above.

Core galaxies are those that exhibit a well defined “break radius,” r_b , which marks a rapid transition (moderated by α) from the outer steep envelope brightness profile (which has asymptotic slope β) to a shallow cusp in surface brightness that generally persists as $r \rightarrow 0$. The break radius also marks the point of maximum curvature of the profile in logarithmic coordinates, and can thus be readily recognized by non-parametric means in addition to the use of the Nuker law. In quantitative terms, core galaxies have $\gamma' < 0.3$. The present sample contains 117 core galaxies.

Power-law galaxies retain a steep slope into the resolution limit, having $\gamma' > 0.5$. These systems are also well described by the Nuker law, but the breaks are poorly defined with small α , or have γ only slightly smaller than β . The “power-law” appellation reflects the appearance of the brightness profiles of these systems in logarithmic coordinates. None of them are truly constant power-laws; they generally have modest decreases in slope as $r \rightarrow 0$. The present sample contains 89 power-law galaxies.

As Lauer et al. (1995) emphasized, we prefer to consider power-laws as galaxies that have no core resolved, rather than presuming that the galaxies intrinsically lack cores. A small number of galaxies classified as power-laws from WFPC1 or NICMOS observations, for example, did reveal cores with the improved resolution of WFPC2 (see the notes in Table 2). The power-law classification thus depends on context. Since most cores measured so far have $r_b < 1$ kpc, clearly the

physical resolution must be much better than this for the non-resolution of a core, and hence the power-law classification, to be interesting. Conversely, the power-law classification has proved to be most intriguing for those galaxies with upper limits on r_b well below those typical to galaxies of similar luminosity.

The sample also contains 13 galaxies that have $0.3 < \gamma' < 0.5$, which, following Rest et al. (2001), are classified as “intermediate” galaxies. These systems are discussed further in §3.3.

3.2. Tests for Bimodality

As noted in the introduction, bimodality has been confirmed in work conducted subsequent to Faber et al. (1997), with the exception of the Ferrarese et al. (2006) VCS results. With the our combined large sample, we can now revisit the overall distribution of γ' and retest the hypothesis that core and power-law galaxies can be described as two distinct populations. This is especially interesting as work by Rest et al. (2001), Ravindranath et al. (2001), and Lauer et al. (2005) has identified a number of “intermediate” galaxies that have $0.3 < \gamma' < 0.5$, thus falling between the core and power-law classes.

The composition of the sample is well suited to the task of exploring bimodality, even though it is a composite of several *HST* samples. We are essentially using most of the nearby early-type galaxy observations that could contribute to such a test. The overall luminosity distribution of the sample is shown in Figure 1. The sample is richest at just the luminosities required to explore the power-law/core transition, and falls off smoothly at both the bright and faint ends. The bright end of the sample is enhanced by the inclusion of BCGs, but as discussed below, we can test subsamples that exclude the BCGs directly, or all bright galaxies at large distances. We can also examine bimodality in a luminosity slice at the power-law/core transition luminosity, to counter concerns about the completeness of the sample at fainter and brighter luminosities. A separate concern might be the potential effects of different physical resolution limits within the sample, given that the galaxies are observed at a variety of distances, particularly if power-law galaxies are classified as such due to insufficient resolution. Faber et al. (1997) showed in their sample, however, that upper limits on the break radii for power-law galaxies fall well below the mean $r_b - L$ relationship at a given luminosity. This remains true in the present sample (Lauer et al. 2007) for all but the faintest power-law galaxies. Power-law galaxies are not simply poorly resolved core galaxies.

Table 2 lists adopted γ' values for the galaxies. Figure 2 shows the new distribution of γ' as a function of r_b in angular units. The overall impression is that the distribution of γ' remains strongly bimodal, even though several galaxies now clearly fall within $0.3 < \gamma' < 0.5$. The bimodality of the complete sample is strongly evident in the histogram of γ' presented in Figure 3.

Rather than just relying on a visual assessment of bimodality, however, we can test for the statistical likelihood of bimodality using the KMM test described by Ashman et al. (1994). The

KMM test compares the likelihood that the frequency distribution of a single parameter is drawn from the sum of two distinct gaussians versus a single gaussian distribution. As Ashman et al. (1994) discuss, the most statistically rigorous test requires that the two gaussians in the bimodal composite distribution have the same dispersion, but the KMM algorithm can relax this assumption; we test the γ' distribution both ways. Table 3 presents the gaussian parameters describing the distribution of γ' shown in Figure 2; the total distributions for equal and unequal dispersions are also plotted in the figure. The KMM test confirms in both cases that the likelihood that γ' was drawn from a single gaussian rather than a bimodal distribution is $< 10^{-3}$. In both cases the two gaussians correspond closely to the core and power-law definitions, with the “valleys” in the distributions falling in the region containing the intermediate galaxies. The “power-law gaussian” is 95% complete for $\gamma' > 0.50$, while the “core gaussian” is 95% complete for $\gamma' < 0.36$.

A different test for bimodality is provided by the DIP Test (Hartigan & Hartigan 1985), which compares the best-fitting unimodal distribution function to the empirical distribution function. The DIP statistic is the maximum difference between these two distribution functions, which is a measure of the multimodality of the sample. Monte Carlo simulations drawn from a unimodal distribution determine the probability of obtaining a measured dip statistic. The DIP Test allows for greater generality in the possible forms of the distribution function, and thus is a more conservative statistic for excluding unimodality. The value of the DIP statistic for the full sample is 0.047, which excludes the unimodal hypothesis at 99.9% significance.

One caveat is that the overall distribution of γ' is biased due to the inclusion of the Laine et al. (2002) BCG sample, which greatly enhances the population of luminous core galaxies. Figures 4 and 5 plot γ' as a function of distance and luminosity, respectively, allowing some potential biases in the complete sample to be explored. Figure 4, for example, shows a strong transition in the population of structural types at $D \approx 50$ Mpc. Since all but two BGC have $D > 50$ Mpc, we can easily exclude them from the sample by considering only those galaxies at $D \leq 50$ Mpc; this cut also excludes several other luminous core galaxies. The smoothed histogram of the distance-cut subsample shown in Figure 3 is clearly bimodal, which is verified by the KMM test; again the likelihood that the population was drawn from a single gaussian is $< 10^{-3}$. The valleys between the two modal peaks for both the equal and unequal dispersion cases are not quite as deep (the distributions are plotted in Figure 4), but the location of the two modal peaks for galaxies with $D \leq 50$ Mpc are essentially the same as those for the entire sample. The value of the DIP statistic for this subsample is 0.050, which excludes the unimodal hypothesis at 98.2% significance.

The transition between power-law and core galaxies that occurs with increasing luminosity is evident in Figure 5; we show the histograms of the structural types with luminosity in Figure 1. While the sample has poor completeness at low luminosities, and the high luminosity population is enhanced by inclusion of the BCG sample, there are no obvious biases in the middle part of the distribution. The figure shows that core and power-law galaxies coexist in roughly equal numbers in the interval $-22.5 < M_V \leq -20.5$, with the occurrence of power-law galaxies dropping off rapidly at higher luminosities, and few core galaxies existing below the low end of this interval. A complete

transition in form occurs over a very small luminosity interval.

The distribution of γ' remains bimodal within the luminosity interval of the power-law/core transition, as is evident in Figure 3. Even though a majority of the intermediate galaxies fall within this luminosity range, they are still relatively rare. One cannot describe the population of galaxies as being drawn from a simple linear relationship between luminosity and γ' . Once again the KMM test rejects the single gaussian at the $< 10^{-3}$ level for representing the distribution of γ' for just the galaxies with $-22.5 < M_V \leq -20.5$. Again, the modal peaks shown in Table 3 and Figure 5 closely correspond to the core and power-law definitions. The value of the DIP statistic for this luminosity-cut subsample is 0.053, which excludes the unimodal hypothesis at 95.5% significance.

3.3. Intermediate Galaxies

The intermediate classification appears to be highly dependent on resolution, as Rest et al. (2001) noted. Indeed, we consider all the galaxies so classified by Rest et al. to be core galaxies, given the finer resolution limits adopted here for their WFPC2 profiles. At the same time, we consider NGC 2902, 4482, 5796, and 5898, which were classified as power-laws by Rest et al., to be intermediate galaxies. Likewise, we find the intermediate classification in the Ravindranath et al. (2001) sample to vary with choice of resolution limit. In a sense, the tests conducted above might lead one to relabel the intermediate galaxies with $0.3 < \gamma' < 0.5$ as “ambiguous galaxies.” The valley in a bimodal distribution is a region where outliers from each mode coexist and classification of any given galaxy cannot be done with any degree of reliability. It is likely that with better resolution some of the present intermediate galaxies would be classified as core galaxies. NGC 3585 and 4709, for example, have well-defined breaks, but have γ' of 0.31 and 0.32, respectively, falling only just above the core boundary; they would probably fall below it with better resolution.

At the same time, we are left with the real physical question of why intermediate galaxies are rare, and the possibility that in at least some cases their central structure may offer a unique window on the problem of core formation. As Rest et al. noted, many intermediates have small α , and do not show as strong breaks as the core galaxies, even accounting for the higher γ values. In the present sample we have difficulty identifying any galaxy with $\gamma' \approx 0.4$ that shows a sharp break and well-defined inner cusp — the best candidates for this appear to be NGC 2902, 5796, and 5898. To explore the utility of the intermediate classification we choose to preserve the 13 intermediate galaxies in the sample as a separate class. This appears to be sensible based on the central parameter relationships presented in Lauer et al. (2007); the intermediate galaxies do not appear to fall on the relationships defined by core galaxies.

4. A Non-Parametric Demonstration of Bimodality in Space Density

Parametric models provide a means to represent data in a simple way that allows one to determine underlying physical relationships. However, care has to be taken so that unknown biases in the parameterization do not affect the overall results. This concern is especially important when studying the luminosity density. Since it is calculated by deprojecting the surface brightness profile, any biases in the brightness profile model will be amplified. Luminosity density is more fundamental than surface brightness, thus it is important to verify that the bimodality of cusp slopes in projection truly reflects the intrinsic distribution of space-density slopes. We therefore bolster the result in the previous section with a non-parametric approach.

The uncertainties for non-parametric models will generally be larger than those resulting from parameter fits, and should provide a more realistic estimate. The comparison between the two approaches was done in Gebhardt et al. (1996), where we found that the Nuker law provides an accurate estimate of the surface brightness profile in the central regions of early-type galaxies. While detailed analysis of the luminosity density, including dynamical studies, should incorporate a non-parametric approach, use of the Nuker law facilitates comparison with theoretical models and parameter correlation studies. Therefore, both are appropriate.

We follow the same procedures as in Gebhardt et al. (1996) to estimate the surface brightness and luminosity density profiles. The technique represents the measured brightness profiles with smoothing splines, and then inverts the splines into density space. Monte Carlo simulations are used to establish the errors in the final density profiles. As the present analysis is identical to that of Gebhardt et al. (1996), we refer the reader to that paper for a complete description.

Figure 6 shows the luminosity density profiles normalized in both radius and luminosity density of all galaxies for which we had the measured isophotal parameters (the Lauer et al. 1995, Lauer et al. 2005, and Laine et al. 2002 samples). The normalization is at the radius that shows the largest logarithmic second derivative in the surface brightness profile; this point corresponds to the break radius in a Nuker law fit, but again it is determined in this context non-parametrically. This plot is analogous to Figure 3 in Gebhardt et al. (1996); however, the Gebhardt et al. (1996) sample only contained 42 galaxies, whereas the present plot is based on 85 galaxies. The two main points evident from both plots are that nearly all galaxies show a central cusp in the luminosity density and that galaxies separate into two types: strong and weak cusp (i.e., power-law and core galaxies).

Again, Figure 6 shows only a subset of the composite sample constructed in this paper, comprising the profiles of Lauer et al. (1995), Faber et al. (1997), and Lauer et al. (2005) for which we have the directly measured WFPC1 or WFPC2 surface photometry. We have excluded the BCGs from Laine et al. (2002), but their inclusion mainly adds core galaxies. The sample in Figure 6 contains more galaxies in the transition region between the core and power-law types than did the sample in Gebhardt et al. (1996), but the statistical difference between the two profile classifications remains as strong. We have checked whether dust has an effect by excluding galaxies with central dust strengths greater than 1.0 (Lauer et al. 2005). The resulting composite plot (the lower panel

in Figure 6) shows even cleaner bimodality in the luminosity density compilation.

We have measured the value of the density logarithmic slope at various radii to determine the significance of the bimodality. We plot histograms and density estimates of the slopes of luminosity density measured at various radii in Figure 7. For these plots, we now include all 166 galaxies for which we have measured profiles. Overplotted on the histograms are adaptive kernel density estimates and their 68% confidence bands (Silverman 1986). As one goes to larger radii to measure the slope, the significance of the two peaks lessens, and beyond $r = 0''.5$ we find a unimodal distribution of slopes. There are many statistical tests to determine the significance of bimodality, and most give very similar results. Using the DIP test For the four radial limits presented ($r = 0''.0, 0''.1, 0''.2,$ and $0''.5$), we find significance values of 0.997, 0.98, 0.80, and 0.40. The hypothesis that the central slopes are unimodal at the *HST* resolution limit is highly excluded, with significance very similar to what we find from the Nuker fits using the KMM algorithm.

5. A Comparison to the ACS Virgo Cluster Survey Profiles

The analysis in the previous sections conflicts strongly with the Ferrarese et al. (2006) conclusion that a bimodal cusp distribution is “untenable.” Ferrarese et al. (2006) derived surface photometry profiles of 100 early-type galaxies in the Virgo cluster as part of their ACS Virgo cluster survey. Their methodology differs from ours in a variety of ways. They used the ACS/WFC, observed in the SDSS g and z filters, and measured surface photometry as a function of isophote geometric mean radius; however, all of these differences are trivial. A more significant difference is that the Ferrarese et al. (2006) sample extends to much fainter systems than we have studied, while we have much richer coverage of bright ($M_V < -19$) systems where the core/power-law transition occurs. The relationship of the central structure of the faint dwarf elliptical galaxies studied in the VCS to that of brighter ellipticals is an important question, but as we discuss later, it is also one that can be cleanly separated from the physical interpretation of bimodality that we have advanced in Faber et al. (1997), namely that at $M_V \approx -21$, the central structure of elliptical galaxies makes a rapid transition in form with increasing luminosity, which is well correlated to other physical properties of the systems. The VCS analysis also finds that core galaxies appear above this luminosity, but their physical picture of less luminous galaxies is markedly different than ours.

The divergence between us and Ferrarese et al. (2006) appears to be mainly due to differences in our respective models used to describe the inner surface brightness profiles of ellipticals. We fit Nuker laws directly to profiles measured from PSF-deconvolved images. Ferrarese et al. (2006) use three different forms, but in all cases are fitting PSF-convolved models to the images as observed. One model uses the Sérsic (1968) form alone,

$$I(r) = I_e \exp \left[-b_n \left(\left(\frac{r}{r_e} \right)^{1/n} - 1 \right) \right], \quad (3)$$

while a second includes an additional King-model nucleus added to this form. For their core

galaxies, Ferrarese et al. (2006) use Core-Sérsic models (Graham et al. 2003), but with $\alpha = \infty$, which mean the galaxies are actually fitted with two different forms that intersect at the break radius,

$$\begin{aligned}
 I(r) &= I_b (r_b/r)^\gamma, & r \leq r_b, \\
 &= I_b \exp \left[b_n \left((r_b/r_e)^{1/n} - (r/r_e)^{1/n} \right) \right], & r > r_b.
 \end{aligned}
 \tag{4}$$

While there are *a priori* reasons for why one might prefer one approach to the other, the only real issue is which approach has better fidelity to the data. A direct comparison of the VCS models and Nuker law fits to deconvolved brightness profiles shows that the Nuker models are superior representations of the observations. Further, the differences between these models and our data are always echoed in the model residuals presented by Ferrarese et al. (2006) for their own data (except where the VCS model includes a large nuclear component, which absorbs the residuals). We conclude that our different results for the same galaxies are not due to differences in the basic image data, nor even the use of deconvolution versus PSF-convolved model fitting (although recognizing subtle systematic failures of the models is considerably more difficult in the observed domain), but in the accuracy and appropriateness of the different profile parameterizations used.

5.1. A Comparison of VCS and Nuker γ' Values for Galaxies in Common

The present sample has 27 galaxies in common with the 100 VCS galaxies. As these are preferentially brighter systems, the overlap between the two samples in the luminosity range associated with the transition between core and power-law galaxies is much more significant; the great majority of the common systems are brighter than the median VCS galaxy luminosity. Of the 27 galaxies, 22 were observed by us in the course of our own *HST* observational programs. The majority of these were imaged with WFPC2, but a substantial minority were obtained with WFPC1. As discussed in Lauer et al. (2005), deconvolved profiles obtained with both cameras agree extremely well for $r > 0''.1$; we show below that both cameras also agree as well with deconvolved ACS/WFC observations. Differing resolution between the three cameras is not a factor that contributes to the differences between the present and VCS results.

Figure 8 plots γ' values from the present sample against those of the VCS sample for the 27 galaxies in common. The agreement between the samples is poor, but there are clear trends in the pattern of the differences. The VCS γ' values for the core galaxies are always systematically higher than our values, while the VCS γ' values for the power-law galaxies are uniformly lower. The dynamic range of the VCS γ' values is thus overall smaller than ours, and many of the VCS γ' values place the galaxies in the intermediate zone between cores and power-laws. In a number of cases, often where Ferrarese et al. (2006) claimed the existence of large nuclei, the agreement between the two samples is especially poor, with the VCS γ' values falling in the range of core galaxies for systems that we had classified as power-laws.

5.2. A Comparison of Deconvolved ACS, WFPC1, and WFPC2 Profiles

The ACS/WFC imagery used by the VCS study and the WFPC2 and WFPC1 imagery that dominate the present sample provide essentially equivalent information. A comparison of WFPC2/PC1 and ACS/WFC PSFs shows that WFPC2 actually provides significantly better angular resolution (Figure 9). The FWHM of the WFPC2/PC1 F555W is $0''.061$, while that of the ACS/WFC F475W PSF is $0''.092$, or 50% larger. The use of *Drizzle* (Fruchter & Hook 2002) to rectify the ACS images slightly degrades its resolution further. The present sample has 49 galaxies at Virgo distance or closer, and a substantial number that are no more than 50% more distant; both the present and VCS samples are probing the same physical scales in the galaxies.

Regardless of the resolution difference between WFPC2 and ACS, PSF-deconvolution provides a model-independent approach to correct *HST* imagery for the “wings” of the PSF outside the *HST* diffraction limit and to isolate the profile analysis from the residual blurring interior to the diffraction limit that remains even after deconvolution. The deconvolution tests presented in Lauer et al. (1992b), Lauer et al. (1995), Lauer et al. (1998), Rest et al. (2001), and Lauer et al. (2005) have established that this methodology works well for *HST* studies of brightness profiles; they also yield well-understood resolution limits. The ACS images can be deconvolved as well to correct for differences between the ACS and WFPC2 PSFs outside the resolution limit. We demonstrate this with direct comparisons of deconvolved ACS and WFPC2 or WFPC1 profiles for several galaxies in common.

Figure 10 compares profiles measured from PSF-deconvolved ACS F475W “drizzled” images to those obtained from deconvolved WFPC1 F555W images (Lauer et al. 1995) for eight galaxies in common, and from deconvolved WFPC2 F555W images (Lauer et al. 2005) for two galaxies in common. We present more extensive comparisons between ACS and WFPC1 than between ACS and WFPC2 because this is the more challenging test; the WFPC1 imagery was blurred by a strongly aberrated PSF. Further, most of the power-law galaxies in common with the VCS sample were observed with WFPC1 rather than WFPC2; the steep central cusps in power-laws present a greater challenge for deconvolution than do core galaxies.

The agreement between all three cameras in all cases is excellent, with differences between the profiles for $r > 0''.1$ limited to only a few percent. This is consistent with the expectations from the simulations and tests quoted above, which show that WFPC1 deconvolutions are largely accurate into $r \approx 0''.1$ (with the caveat noted in Lauer et al. 2005 that WFPC1 deconvolutions may be less accurate at this radius if a strong nuclear point source is present). ACS/WFC has superior resolution for $r < 0''.1$, as evidenced by the systematically higher central surface brightnesses recovered interior to this radius. Since Figure 10 shows nearly all of the 10 WFPC1 overlap galaxies⁴, it demonstrates directly that the use of WFPC1 profiles in the present sample is not a

⁴We exclude NGC 4434, for which the archived drizzled-image has a strong artifact in the galaxy center, and NGC 4486, which is a core galaxy, and for which Lauer et al. (1992a) removed the nuclear non-thermal source from the

factor in the strongly different γ' values derived from the Nuker and VCS models.

The two galaxies selected for the WFPC2/ACS comparisons are the most centrally compact galaxies observed with WFPC2 in the overlap sample, and thus are the most sensitive to differences in resolution. The WFPC2 profiles show superior resolution to ACS/WFC for $r < 0''.1$, which is expected, given the sharper WFPC2 PSF. Again, however, none of the differences between the VCS results and ours depends on the exquisite treatment of details near the *HST* diffraction limit, as we will show in the next section.

5.3. Comparison of Nuker Laws and VCS Profile Models for Galaxies in Common

The VCS and present γ' values both come from models of the galaxy intrinsic light distributions. Understanding the differences between the γ' values shown in Figure 8 requires comparing the VCS and Nuker intrinsic models to the deconvolved surface brightness profiles, which are themselves a non-parametric representation of the intrinsic light distributions of the galaxies. The concordance between ACS and WFPC2 or WFPC1 deconvolved profiles further means that we can directly compare the VCS intrinsic profile models (the adopted representation of the profiles *prior* to PSF convolution) to the deconvolved WFPC2 or WFPC1 profiles, as well as comparing the Nuker models to deconvolved ACS/WFC profiles. In practice, we can select the camera that provides the highest spatial resolution for a given galaxy, thus comparing both the Nuker and VCS models to the best deconvolved profile of the galaxy. In general, this means using WFPC2 profiles as the first choice, with the ACS as the second choice (WFPC1 profiles will still be used for the two exceptions noted above).

The disagreement of γ' values shown in Figure 8 can be traced to differences between the VCS and Nuker profile models. We show this on a galaxy by galaxy basis in Figures 11 to 13 by comparing the published *intrinsic* VCS *g*-band models and Nuker models to WFPC2, ACS, and WFPC1 deconvolved isophotal brightnesses. The measured brightness values are presented twice. The lower trace has the isophotal scale converted to mean radii to accommodate the VCS models, which are normalized to the surface brightness measures at $r > 2''$ to account for the color offset between the WFPC1/2 F555W and ACS F475W filters. The upper traces are the same data offset by 0.5 mag and fitted with the Nuker models using our preferred semi-major axis radial scale (these plots were shown earlier in either Byun et al. 1996 or Lauer et al. 2005). Note that the Nuker laws often are not fitted all the way into $r = 0$. The limits shown are those we have adopted to avoid central nuclei, and so on, and when larger than the general resolution limits presented in §2 are always the scale at which we measured γ' . Because we are working in the deconvolved domain, we can exclude the points interior to some radial limit from the fit. In contrast, models fitted to PSF-convolved images must always account for the flux at $r = 0$, given its contribution to larger

WFPC1 images.

radii in the observed domain. We thus show the VCS models into the smallest radii for which isophotal parameters have been measured.

We do not present any quantitative measure of how well the Nuker versus VCS models fit the data — simple examination of Figures 11 to 13 shows that the Nuker fits provide a better representation of the data in all 22 galaxies. The differences between the Nuker and VCS models can be better understood by grouping the galaxies into three sets: galaxies classified having core type profiles in this paper, galaxies classified as power-law profiles in this paper for which Ferrarese et al. (2006) did not include a nuclear component, and power-laws for which they did include a nucleus.

5.3.1. VCS Models of Core Galaxies

Ferrarese et al. (2006) described the profiles of the most luminous core galaxies (NGC 4365, 4382, 4406, 4472, 4486, 4552, and 4649) with the Graham et al. (2003) Core-Sérsic model, which features a power-law cusp at small radii transitioning to a Sérsic model at large radii. As with the Nuker law, the radial extent or smoothness of the transition is moderated by the α parameter. Ferrarese et al. (2006), however set $\alpha = \infty$, causing a sharp unphysical slope discontinuity the break radius, r_b , which sets the radius of transition between the inner cusp and outer Sérsic law.⁵ Setting $\alpha = \infty$ also forces a cusp of constant logarithmic slope to be fitted for all $r < r_b$.

As is clear in Figure 11, the inner profiles of the core galaxies curve downward as they make a smooth transition from the shallow central cusps to the steeper envelopes. This transition is well described by the Nuker law; indeed Lauer et al. (1995) emphasized the need for allowing α to be a free parameter. Force-fitting a cusp with constant logarithmic slope for $r < r_b$ yields a γ' value that represents the average slope interior to r_b . As the slope typically continues to decrease as $r \rightarrow 0$, the true γ' at the resolution limit (or terminus of the Nuker-law fit) will be systematically smaller, explaining the systematic effect seen in Figure 8.

The departures of the VCS models from the WFPC2 data appear to be completely consistent their residuals from the original ACS/WFC data as well. The patterns produced by assuming the inner cusp to have constant slope are readily evident in the residual traces presented in Figure 103 of Ferrarese et al. (2006). Because that figure only presents residuals in the observed domain, the systematic trends are more subtle than those evident in Figure 11; however, one always sees a sharp bump at $r = r_b$, with a nonzero residual slope at smaller radii.

In the cases of NGC 4473, 4478, and 4486B, Ferrarese et al. (2006) fitted Sérsic models to

⁵While the r_b parameter in the Core-Sérsic law serves an analogous role to the Nuker break radius, r_b , they are not mathematically equivalent and cannot be compared directly. The Nuker r_b occurs at the point of maximum profile curvature (in log-log coordinates), while for the Core-Sérsic form this point is an exceedingly complex expression involving all parameters except the photometric scale.

galaxies that we classified as core systems. NGC 4473 is well described by a Nuker law with a small α parameter. The Sérsic model in contrast clearly over estimates the central γ' ; again the pattern of residuals that we see here is obvious in VCS Figure 103 as well. This is also true for NGC 4486B. The extremely large residuals from the Sérsic fit for NGC 4478 seen in Figure 11 are again echoed in VCS Figure 103. While we concluded that NGC 4478 has a small nucleus (Lauer et al. 2005), no such component was included in the VCS model fits. Lastly, one low-luminosity core galaxy, NGC 4458, was fitted with a highly luminous and spatially extended nucleus by Ferrarese et al. (2006); it will be discussed in the context of other galaxies with large assumed VCS nuclei below.

We conclude that none of the present core galaxies observed in the VCS are well matched by the VCS models as the resolution limit is approached. The VCS choice of a cusp with a constant inner slope or fitting a Sérsic model to galaxies with small cores always results in higher γ' values than result from the Nuker parameters.

5.3.2. VCS Sérsic Models of Power-law Galaxies

NGC 4434, 4464, 4621, and 4660 are galaxies that we have classified as power-laws that Ferrarese et al. (2006) fitted with pure Sérsic laws. The VCS models for all four galaxies fall below the data as $r \rightarrow 0$ (Figure 12). Again, this behavior is echoed in VCS Figure 103, which shows that the Sérsic fits fall below the *observed domain* ACS VCS data for $r < 0''.3$ in NGC 4464, 4621, and 4660, and $r < 0''.15$ in NGC 4434. Ferrarese et al. (2006) note that the ACS F475W images of both NGC 4621 and 4660 are actually centrally saturated. This is problematic as information about the central structure is lost once saturation occurs, but it still must be accounted for in the profile models, given that light from the center is also conveyed to larger radii by the PSF. In contrast the Nuker models nicely match all four galaxies, In the case of NGC 4464 it is especially notable that the Nuker profile, which was derived from WFPC1 imagery, has better fidelity to the ACS profile than the VCS model derived directly from the same data.

The plot of Nuker γ' versus VCS γ' in Figure 8 contains two more power-law galaxies, NGC 4417 and 4564, for which we do not have our own WFPC2 or WFPC1 profiles, but again the residuals in VCS Figure 103 show that their Sérsic models fall well below the ACS data as $r \rightarrow 0$. This appears to be a generic feature of nearly all the VCS galaxies modelled as non-nucleated Sérsic profiles, looking at the VCS galaxies for which we do not have our own data. NGC 4483, 4528, and 4570 are additional examples of where the departure of the VCS Sérsic models below their own data is especially large as the *HST* resolution limit is approached.

In summary, none of the present power-law galaxies are well matched by the VCS pure Sérsic models as the resolution limit is approached. The Sérsic models always fall below the data at the center, resulting in smaller γ' values than are inferred from the Nuker parameters.

5.3.3. VCS Sérsic + Nucleus Models of Power-law Galaxies

The set of galaxies in Figure 13, NGC 4387, 4467, 4551, VCC 1199, 1440, 1545, and 1627, are power-law galaxies to which Ferrarese et al. (2006) fitted Sérsic laws plus luminous extended nuclear components. Deconvolved ACS images provide all the profiles for this set of comparisons. Lauer et al. (1995) identified nuclei in all these galaxies as well (with the exception of NGC 4467), albeit ones of markedly lower luminosity and extent than those presented by Côté et al. (2006). It is evident from examining the profile fits in Figure 12 that the Nuker laws can accurately describe the deconvolved ACS profiles of these galaxies into small radii, even though all the Nuker models in this subsection were derived from WFPC1 imagery.

The VCS Sérsic + Nucleus Models *in toto* are also excellent models of the data and thus are physically plausible representations, but the total quality of the fit is not relevant to the accuracy of γ' . The VCS Sérsic components *alone*, from which γ' is measured, always fall below the data well before the resolution limit is reached (Figure 13). The implied nuclei often greatly dominate the inner regions where *HST* provides unique resolution, The VCS γ' values for such systems are thus inward extrapolations evaluated at radii that in some cases are over an order of magnitude smaller than radii at which the Sérsic profile actually dominates. In contrast, the γ' values from the Nuker laws always reflect the end point of the radial interval over which the fit was performed. We see no reason why an extrapolated γ' measurement from a Sérsic law fitted to the envelope should be used in preference to the local γ' at the resolution limit provided by the Nuker law.

Côté et al. (2006) point out that definition of what constitutes a nucleus can depend on what the underlying assumed profile is. A corollary of this, however, is that nuclei so identified will not be unique. The prior existence of the Nuker fits, which also assume small nuclei for nearly all for the galaxies listed above, establishes this. It is worth noting that Sérsic models had not been tested for use to describe the inner portions of *HST* brightness profiles prior to the VCS work for more than a few galaxies. The VCS work, however, takes it as an *a priori* assumption rather than as a hypothesis that the envelopes of galaxies, which is where the Sérsic laws are fitted, can be used to deduce the structure of the central profile at small radii. Under this picture, excursions of the data above the Sérsic model are declared to be separate nuclear components, rather than as a simple failure of the model. The VCS nuclei effectively absorb the central flux left over from the Sérsic fits; the residual traces in VCS Figure 103 for such galaxies are nearly flat. As Figure 13 demonstrates, forcing a Sérsic fit to galaxies that truly have slowly decreasing power-law profiles will clearly create ersatz nuclei. Again, we see no physical or even empirical justification to prefer the Sérsic + nucleus model, let alone any demonstration strong enough to show that the Nuker law-based interpretation is untenable.

The Nuker law, of course, has no physical justification either, however, we are not using it to extrapolate beyond the domain of the fit; it serves in this context as a smooth representation of the data. Likewise, the use of Sérsic models is interesting for the portions of the envelope for which they are adequate fits. Neither should be used to extrapolate to radii considerably smaller than

those that are well fitted by their forms — this is why we emphasize the use of γ' , which is always a local measure, in preference to γ , which itself is the slope only realized as $r \rightarrow 0$.

In this context it is interesting to revisit the non-parametrically derived space density profiles in Figure 6. The strong impression of bimodality in this figure is concordant with the parametric analysis based on the limiting projected profile slopes provided by the Nuker law. Under the VCS interpretation, however, the clean separation of the two bundles of profiles in the figure would be interpreted as due to nuclear components in the upper bundle, and the composite plot of “true” galaxy density profiles could only be constructed with reference to the VCS parametric models.

In our analysis of WFPC1 data (Lauer et al. 1995) or WFPC2 data (Lauer et al. 2005), we identified nuclei by looking for upturns above a power-law cusp as $r \rightarrow 0$. These are often obvious in core galaxies, as can be seen in some of the examples in Figure 11, but for power-law galaxies the evidence for a possible nucleus is often just a subtle increase in the profile slope as the resolution limit is approached. There are no strong *upward* breaks in any of the galaxies discussed in this section that would make detection of a nucleus unambiguous. At the same time, Rest et al. (2001) present deconvolved WFPC2 observations of NGC 4474 and 4482, two galaxies that are plotted in Figure 8 with widely differing γ' values, that do have clearly defined nuclei, but again ones more modest than those implied by the VCS models.

We explore the non-uniqueness of the Sérsic + nucleus model in further detail for NGC 4458, in which we plot the Lauer et al. (2005) data for this galaxy extended to large radii by the addition of the B band data of Jedrzejewski (1987) (Figure 14). The Nuker law is fitted to $r < 15''$, or 2.8 decades in radius, a portion of the galaxy that Côté et al. (2006) consider to be a bright and extended nucleus. The Ferrarese et al. (2006) Sérsic fit in contrast is valid over only $4'' < r < 50''$, a little more than a single decade in radius, but is then extrapolated inwards by 1.6 decades to the radius at which Ferrarese et al. (2006) report γ' .

The profile of this object is obviously complex and the Nuker residuals shown in Lauer et al. (2005) show a sinusoidal pattern, associated with an increase in profile slope at $r \approx 1''$. Perhaps by our criterion, this could be interpreted to be the onset of a nucleus. Even so, the Nuker law fitted to just $r > 1''$ would clearly model this region with less curvature than implied by the Sérsic model, again giving a less luminous nucleus. Yet another interpretation, however, is that NGC 4458 is a dwarf S0 galaxy, in which the Nuker law appropriately describes the bulge while the Sérsic law correctly captures the disk. The case of NGC 4458 emphasizes that the use of Sérsic models plus large nuclei is neither unique nor compelling in galaxies of the luminosities that we are considering.

6. Summary

The distribution of surface brightness cusp slopes as the *HST* resolution limit is approached is strongly bimodal. This confirms once again the usefulness of classification of galaxies into core or power-law systems based on their central brightness profiles. Bimodality is still evident for galaxies

within 50 Mpc, or for those restricted in luminosity to $-22.5 < M_V \leq -20.5$. This last result is of particular interest as it is the interval over which the typical central structure of early-type galaxies changes in form. Very few core galaxies have $M_V \geq -20.5$, while only a small number of power-law galaxies have $M_V \leq -22.5$. There are a few galaxies that have profiles with $0.3 < \gamma' < 0.5$, thus placing them in an intermediate position between core and power-law systems. Intriguingly, these galaxies are most common in the luminosity range over which the core/power-law transition occurs. Intermediate galaxies are rare, however, and they do not fill in the “valley” in the distribution of cusp slopes.

As a check on our conclusions that the distribution of cusp slopes is bimodal, we repeated the non-parametric analysis of the *HST* brightness profiles presented by Gebhardt et al. (1996). This provides a strong demonstration of bimodality in the space *density* profiles without reference to any fitting function or any physical assumption beyond adopting the radius of maximum curvature of the profiles as a common physical scale. The concordance of this very simple approach with the results from the Nuker law fits, shows that inferences of bimodality from Nuker law fits alone are not due to artifacts in or poor behavior of its parametric form,

These conclusions are inconsistent with the results of Ferrarese et al. (2006), who presented a strongly different distribution of γ' values based on their VCS galaxies. By examining galaxies in common with the VCS sample, we find that profiles derived from ACS/WFC, WFPC2, and WFPC1 agree extremely well to their stated resolution limits. In contrast, we find that the VCS profile models, which the VCS uses to characterize cusp slopes, are either poor representations of the data as the *HST* resolution limit is approached, or consist of inward extrapolations of forms fitted to the envelope. While the latter case, which requires the assumption of large nuclear clusters, may be a plausible model, it is neither unique nor compelling enough to demonstrate that the previous modeling of profiles conducted by our group and others is “untenable.”

We do note our large composite sample is largely limited to galaxies with $M_V < -19$. The core/power-law transition occurs at still larger luminosities, and our conclusions on bimodality are limited to this context. This luminosity limit corresponds to roughly the median VCS galaxy luminosity, however, and many of the faintest VCS galaxies have profiles that are nearly flat at the center. Ferrarese et al. (2006) are concerned that under our criteria such systems would be classified as cores, something that we have not actually done. The envelope profiles of these galaxies are nearly exponential and have no well-defined breaks as the center is approached⁶. Their overall forms are completely different from the luminous core galaxies and thus they are trivially distinguished from them. Kormendy (1985), Kormendy (1987), and Kormendy & Bender (1994) showed that ellipticals and spheroidals form well defined, disjoint sequences in parameter space. A recent analysis of the profiles of low-luminosity ellipticals and a comparison to a large sample of Sph galaxies strongly confirms the E/Sph dichotomy (Kormendy et al. 2007). The resolution of this

⁶Indeed, the maximum logarithmic second derivative, and hence the location of r_b , is reached only in the limit $r \rightarrow \infty$ for a pure exponential profile.

question, however, is not relevant to the strong physical dichotomy between power-law and core galaxies advanced in Faber et al. (1997). Cores are a phenomenon of the most luminous galaxies. Their likely immediate progenitors are the power-law galaxies of slightly lower luminosity. The distribution of γ' for $M_V < -19$ is the relevant diagnostic for how this transition occurred.

This research was supported in part by several grants provided through STScI associated with GO programs 5512, 6099, 6587, 7388, 8591, 9106, and 9107. Our team meetings were generously hosted by the National Optical Astronomy Observatory, the Observatories of the Carnegie Institution of Washington, the Aspen Center for Physics, the Leiden Observatory, and the University of California, Santa Cruz Center for Adaptive Optics. We thank Steve Zepf for the KMM software. We thank the referee for a careful review of the manuscript. We thank Dr. Laura Ferrarese for her comments on an earlier draft of this paper.

REFERENCES

- Ashman, K. A., Bird, C. M., & Zepf, S. E. 1994, *AJ*, 108, 2348
- Baggett, W. E., Baggett, S. M., & Anderson, K. S. J. 1998, *AJ*, 116, 1626
- Balmaverde, B., & Capetti, A. 2006, *A&A*, 447, 97
- Begelman, M. C., Blandford, R. D., & Rees, M. J. 1980, *Nature*, 287, 307
- Bender, R. 1988, *A&A*, 193, L7
- Bender, R., Saglia, R. P., & Gerhard, O. E. 1994, *MNRAS*, 269, 785
- Bender, R., Surma, P., Doebereiner, S., Moellenhoff, C., & Madejsky, R. 1989, *A&A*, 217, 35
- Boroson, T. 1981, *ApJS*, 46, 177
- Burstein, D. 1979, *ApJ*, 234, 435
- Byun, Y. I., et al. 1996, *AJ*, 111, 1889
- Capetti, A., & Balmaverde, B. 2005, *A&A*, 440, 73
- Carollo, C. M., Franx, M., Illingworth, G. D., & Forbes, D. 1997, *ApJ*, 481, 710
- Côté, P., et al. 2006, *ApJS*, 165, 57
- Crane, P., et al. 1993, *AJ*, 106, 1371
- de Vaucouleurs, G., de Vaucouleurs, A., Corwin, H. G., Buta, R. J., Paturel, G., & Fouque, P. 1991, Volume 1-3, XII, 2069 pp. 7 figs.. Springer-Verlag Berlin Heidelberg New York
- Ebisuzaki, T., Makino, J., & Okumura, S. K. 1991, *Nature*, 354, 212
- Faber, S. M., Tremaine, S., Ajhar, E. A., Byun, Y., Dressler, A., Gebhardt, K., Grillmair, C., Kormendy, J., Lauer, T. R., & Richstone, D. 1997, *AJ*, 114, 1771
- Faber, S. M., Wegner, G., Burstein, D., Davies, R. L., Dressler, A., Lynden-Bell, D., & Terlevich, R. J. 1989, *ApJS*, 69, 763
- Ferrarese, L., van den Bosch, F. C., Ford, H. C., Jaffe, W., & O'Connell, R. W. 1994, *AJ*, 108, 1598
- Ferrarese, L., et al. 2006, *ApJS*, 164, 334
- Fruchter, A. S., & Hook, R. N. 2002, *PASP*, 114, 144
- Gebhardt, K., Richstone, D., Ajhar, E. A., Lauer, T. R., Byun, Y., Kormendy, J., Dressler, A., Faber, S. M., Grillmair, C., & Tremaine, S. 1996, *AJ*, 112, 105

- Gebhardt, K., et al. 2000, *ApJ*, 539, L13
- Graham, A. W., Erwin, P., Trujillo, I., & Asensio Ramos, A. 2003, *AJ*, 125, 2951
- Hartigan, J. A., & Hartigan, P. M. 1985, *Ann. Statist.*, 13, 70
- Jaffe, W., Ford, H. C., O’Connell, R. W., van den Bosch, F. C., & Ferrarese, L. 1994, *AJ*, 108, 1567
- Jedrzejewski, R. I. 1987, *MNRAS*, 226, 747
- Kent, S. M. 1985, *ApJS*, 59, 115
- King, I. R. 1966, *AJ*, 71, 64
- Kormendy, J. 1985, *ApJ*, 295, 73
- Kormendy, J. 1987, *Nearly Normal Galaxies. From the Planck Time to the Present*, 163
- Kormendy, J., & Bender, R. 1994, in *ESO/OHP Workshop on Dwarf Galaxies*, ed. G. Meylan and P. Prugniel (Garching: ESO), p. 161.
- Kormendy, J., & Bender, R. 1996, *ApJ*, 464, L119
- Kormendy, J., Dressler, A., Byun, Y.-I., Faber, S. M., Grillmair, C., Lauer, T. R., Richstone, D., & Tremaine, S. 1994, in *ESO/OHP Workshop on Dwarf Galaxies*, ed. G. Meylan and P. Prugniel (Garching: ESO), p. 147.
- Kormendy, J., Fisher, D. B., Cornell, M. E., & Bender, R. 2007, *ApJS*, submitted
- Kormendy, J., & Gebhardt, K. 2001, *AIP Conf. Proc.* 586: 20th Texas Symposium on relativistic astrophysics, 586, 363
- Kormendy, J., & Illingworth, G. 1983, *ApJ*, 265, 632
- Laine, S., van der Marel, R. P., Lauer, T. R., Postman, M., O’Dea, C. P., & Owen, F. N. 2003, *AJ*, 125, 478
- Lauer, T. R. 1985, *ApJ*, 292, 101
- Lauer, T. R., Ajhar, E. A., Byun, Y.-I., Dressler, A., Faber, S. M., Grillmair, C., Kormendy, J., Richstone, D., & Tremaine, S. 1995, *AJ*, 110, 2622
- Lauer, T. R., Faber, S. M., Ajhar, E. A., Grillmair, C. J., & Scowen, P. A. 1998, *AJ*, 116, 2263
- Lauer, T. R., et al. 1991, *ApJ*, 369, L41
- Lauer, T. R., et al. 1992a, *AJ*, 103, 703
- Lauer, T. R., et al. 1992b, *AJ*, 104, 552

- Lauer, T. R., et al. 2002, *AJ*, 124, 1975
- Lauer, T. R., et al. 2005, *AJ*, 129, 2138
- Lauer, T. R., et al. 2007, *ApJ*, submitted
- Magorrian, J., et al. 1998, *AJ*, 115, 2285
- Makino, J. 1997, *ApJ*, 478, 58
- Milosavljević, M., & Merritt, D. 2001, *ApJ*, 563, 34
- Nieto, J.-L., Bender, R., & Surma, P. 1991, *A&A*, 244, L37
- Pellegrini, S. 2005, *MNRAS*, 364, 169
- Postman, M., & Lauer, T. R. 1995, *ApJ*, 440, 28
- Press, W. H., Teukolsky, S. A., Vetterling, W. T., & Flannery, B. P. 1992, *Numerical Recipes 2d ed.* (Cambridge: Cambridge Univ. Press)
- Quillen, A. C., Bower, G. A., & Stritzinger, M. 2000, *ApJS*, 128, 85
- Ravindranath, S., Ho, L. C., Peng, C. Y., Filippenko, A. V., & Sargent, W. L. W. 2001, *AJ*, 122, 653
- Rest, A., van den Bosch, F. C., Jaffe, W., Tran, H., Tsvetanov, Z., Ford, H. C., Davies, J., & Schafer, J. 2001, *AJ*, 121, 2431
- Ryden, B. S., Forbes, D. A., & Terlevich, A. I. 2001, *MNRAS*, 326, 1141
- Sérsic, J. L. 1968, Cordoba, Argentina: Observatorio Astronomico, 1968
- Schlegel, D. J., Finkbeiner, D. P., & Davis, M. 1998, *ApJ*, 500, 525
- Silverman, B. W. 1986, *Density Estimation for Statistics and Data Analysis* (New York: Chapman and Hall)
- Simien, F., & de Vaucouleurs, G. 1986, *ApJ*, 302, 564
- Tonry, J. L., Dressler, A., Blakeslee, J. P., Ajhar, E. A., Fletcher, A. B., Luppino, G. A., Metzger, M. R., & Moore, C. B. 2001, *ApJ*, 546, 681
- Tremblay, B., & Merritt, D. 1996, *AJ*, 111, 2243

Table 1. Global Parameters

Galaxy	Morph	D (Mpc)	Ref	M_V	R_e log(pc)	S	Notes
NGC 0404	S0–	3.5	1	–17.19	3.17	6	$\Delta M = 0.45$ (1)
NGC 0474	S0	29.3	2	–20.12	3.59	6	$\Delta M = 0.82$ (2)
NGC 0507	S0	63.8	4	–23.02	4.11	1	
NGC 0524	S0+	25.4	1	–21.85	...	5	$\Delta M = 0.19$ (2)
NGC 0545	BCG	73.3	2	–22.98	4.36	3	A0194-M1
NGC 0584	E	22.1	1	–21.38	3.53	1	
NGC 0596	E	22.1	1	–20.90	3.51	1	
NGC 0720	E	29.2	1	–22.20	3.80	4	
NGC 0741	E	70.9	4	–23.27	4.12	1	
NGC 0821	E	25.5	1	–21.71	3.56	1	
NGC 0910	BCG	81.1	2	–22.79	4.19	3	A0347-M1
NGC 1016	E	75.9	3	–22.90	...	1	
NGC 1023	S0–	12.1	1	–20.53	...	1	$\Delta M = 0.73$ (3)
NGC 1052	E	20.5	1	–21.17	3.52	5	
NGC 1172	E	22.7	1	–20.13	3.64	4	
NGC 1316	E	22.7	1	–23.32	3.86	1	
NGC 1331	E	24.2	1	–18.58	...	5	
NGC 1351	S0–	21.0	1	–20.08	3.62	5	
NGC 1374	E	20.9	1	–20.57	3.41	1	
NGC 1399	E	21.1	1	–22.07	3.62	1	
NGC 1400	S0–	26.5	1	–21.37	3.47	4	$\Delta M = 0.00$ (1)
NGC 1426	E	26.5	1	–20.78	3.56	1	
NGC 1427	E	21.0	1	–20.79	3.50	1	
NGC 1439	E	26.5	1	–20.82	3.61	1	
NGC 1500	BCG	132.5	2	–22.75	4.19	3	A3193-M1
NGC 1553	S0	21.0	1	–22.06	...	5	$\Delta M = 0.19$ (4)
NGC 1600	E	57.4	2	–23.02	4.13	4	
NGC 1700	E	40.6	2	–21.95	3.64	1	
NGC 2300	S0	30.4	4	–21.74	3.70	1	
NGC 2434	E	22.8	1	–21.33	3.56	1	
NGC 2549	S0	13.4	1	–19.17	3.37	2	$\Delta M = 0.46$ (1)
NGC 2592	E	27.2	1	–20.01	...	2	

Table 1—Continued

Galaxy	Morph	D (Mpc)	Ref	M_V	R_e log(pc)	S	Notes
NGC 2634	E	35.3	1	−20.83	...	2	
NGC 2636	E	38.3	2	−19.19	...	4	
NGC 2685	S0+	14.3	2	−19.72	...	6	$\Delta M = 0.00$ (1)
NGC 2699	E	28.4	1	−20.25	...	2	
NGC 2778	E	24.2	1	−18.75	3.21	1	$\Delta M = 0.82$ (2)
NGC 2832	BCG	96.8	2	−23.76	4.50	3	A0779-M1
NGC 2841	Sb	15.1	2	−20.57	...	4	$\Delta M = 1.54$ (5)
NGC 2872	E	47.4	2	−21.62	...	2	
NGC 2902	S0	33.0	2	−20.59	...	2	$\Delta M = 0.00$ (1)
NGC 2907	Sa	34.4	4	−21.23	...	5	$\Delta M = 0.00$ (1)
NGC 2950	S0	15.8	1	−19.73	3.19	2	$\Delta M = 0.38$ (1)
NGC 2974	E	22.7	1	−21.09	3.61	1	
NGC 2986	E	37.6	2	−22.32	3.83	2	
NGC 3056	S0+	12.9	1	−18.98	...	5	$\Delta M = 0.19$ (1)
NGC 3065	S0	29.6	2	−19.64	3.36	2	$\Delta M = 0.35$ (1)
NGC 3078	E	37.2	1	−21.95	...	2	
NGC 3115	S0−	10.2	1	−21.11	3.37	1	$\Delta M = 0.19$ (3)
NGC 3193	E	36.0	1	−21.98	3.63	2	
NGC 3266	S0	29.4	2	−20.11	...	2	
NGC 3348	E	41.5	2	−22.18	...	2	
NGC 3377	E	11.7	1	−20.07	3.30	1	
NGC 3379	E	11.7	1	−21.14	3.39	1	
NGC 3384	S0−	11.7	1	−19.93	3.08	1	$\Delta M = 0.58$ (6)
NGC 3414	S0	26.7	1	−20.25	3.63	2	$\Delta M = 0.97$ (1)
NGC 3551	BCG	130.1	2	−23.55	4.79	3	A1177-M1
NGC 3585	E	21.2	1	−21.93	...	1	
NGC 3595	E	35.2	2	−20.96	...	2	
NGC 3599	S0	23.0	1	−19.93	...	4	
NGC 3605	E	23.0	1	−19.61	3.20	4	
NGC 3607	S0	10.9	1	−19.88	3.28	1	$\Delta M = 0.48$ (1)
NGC 3608	E	23.0	1	−21.12	3.52	1	
NGC 3610	E	22.6	1	−20.96	3.16	1	

Table 1—Continued

Galaxy	Morph	D (Mpc)	Ref	M_V	R_e log(pc)	S	Notes
NGC 3613	E	30.8	1	−21.59	3.80	2	
NGC 3640	E	28.3	1	−21.96	3.69	1	
NGC 3706	S0−	46.9	4	−22.31	3.90	1	
NGC 3842	BCG	97.0	4	−23.18	4.25	1	A1367-M1
NGC 3900	S0+	29.9	2	−20.80	...	6	$\Delta M = 0.33$ (1)
NGC 3945	S0+	19.9	3	−20.25	...	1	$\Delta M = 0.49$ (1)
NGC 4026	S0	15.6	1	−19.79	3.59	1	$\Delta M = 0.50$ (1)
NGC 4073	E	92.2	4	−23.50	...	1	
NGC 4121	E	25.2	1	−18.53	...	2	
NGC 4128	S0	34.5	2	−20.79	3.48	2	
NGC 4143	S0	15.6	1	−19.68	3.13	6	$\Delta M = 0.59$ (1)
NGC 4150	S0	14.5	1	−18.66	...	5	$\Delta M = 0.57$ (1)
NGC 4168	E	37.3	2	−21.80	3.92	2	
NGC 4239	E	17.5	2	−18.50	...	4	
NGC 4261	E	33.4	1	−22.26	3.91	5	
NGC 4278	E	16.7	1	−21.05	3.39	1	
NGC 4291	E	25.0	1	−20.64	3.29	1	
NGC 4365	E	21.6	1	−22.18	3.89	1	
NGC 4374	E	17.9	1	−22.28	3.75	5	
NGC 4382	S0+	17.9	1	−21.96	3.81	1	$\Delta M = 0.29$ (1)
NGC 4387	E	17.9	1	−19.25	3.23	4	
NGC 4406	E	17.9	1	−22.46	4.09	1	
NGC 4417	S0	17.9	1	−18.94	3.50	6	$\Delta M = 1.30$ (1)
NGC 4434	E	17.9	1	−19.19	...	4	
NGC 4458	E	17.9	1	−19.27	...	1	
NGC 4464	E	17.9	1	−18.82	...	4	
NGC 4467	E	17.9	1	−17.51	...	4	
NGC 4472	E	17.9	1	−22.93	3.94	1	
NGC 4473	E	17.9	1	−21.16	3.42	1	
NGC 4474	S0	21.6	1	−18.42	3.30	2	$\Delta M = 1.89$ (1)
NGC 4478	E	17.9	1	−19.89	3.13	1	
NGC 4482	E	17.9	1	−18.87	...	2	

Table 1—Continued

Galaxy	Morph	D (Mpc)	Ref	M_V	R_e log(pc)	S	Notes
NGC 4486	E	17.9	1	−22.71	3.94	4	
NGC 4486B	cE	17.9	1	−17.98	...	1	
NGC 4494	E	17.9	1	−21.50	3.57	1	
NGC 4503	S0−	17.9	1	−19.57	...	2	$\Delta M = 0.79$ (1)
NGC 4551	E	17.9	1	−19.37	3.32	4	
NGC 4552	E	17.9	1	−21.65	3.55	1	
NGC 4564	E	17.9	1	−20.26	3.44	2	
NGC 4589	E	25.0	1	−21.35	3.71	1	
NGC 4621	E	17.9	1	−21.74	3.57	1	
NGC 4636	E	17.9	1	−21.86	4.02	5	
NGC 4648	E	27.7	1	−20.24	...	2	
NGC 4649	E	17.9	1	−22.51	3.82	1	
NGC 4660	E	17.9	1	−20.13	3.02	1	
NGC 4696	BCG	40.0	2	−24.33	4.52	3	A3526-M1
NGC 4697	E	13.3	1	−21.49	3.71	4	
NGC 4709	E	37.0	1	−22.32	...	1	
NGC 4742	E	16.4	1	−19.90	2.80	4	
NGC 4874	E	106.6	2	−23.49	4.79	4	
NGC 4889	BCG	95.0	2	−23.73	4.40	3	A1656-M1
NGC 5017	E	40.3	2	−20.67	...	2	
NGC 5061	E	26.9	4	−22.01	3.55	1	
NGC 5077	E	44.9	2	−22.07	...	2	
NGC 5198	E	38.3	2	−21.23	...	2	
NGC 5308	S0−	33.0	1	−21.26	3.90	2	
NGC 5370	S0	45.2	2	−20.60	...	2	
NGC 5419	E	62.6	4	−23.37	4.18	1	
NGC 5557	E	52.7	4	−22.62	3.77	1	
NGC 5576	E	27.1	1	−21.31	3.58	1	
NGC 5796	E	45.2	2	−21.98	...	2	
NGC 5812	E	28.4	1	−21.39	...	2	
NGC 5813	E	28.7	1	−22.01	3.94	1	
NGC 5831	E	28.7	1	−21.00	3.53	2	

Table 1—Continued

Galaxy	Morph	D (Mpc)	Ref	M_V	R_e log(pc)	S	Notes
NGC 5838	S0–	22.2	2	–20.51	3.83	6	$\Delta M = 0.45$ (1)
NGC 5845	E	28.7	1	–19.98	2.66	5	
NGC 5898	E	33.3	1	–21.65	...	2	
NGC 5903	E	33.3	1	–21.90	...	2	
NGC 5982	E	40.5	4	–21.97	3.70	1	
NGC 6086	BCG	131.2	2	–23.11	4.37	3	A2162-M1
NGC 6166	BCG	128.6	2	–23.80	4.83	4	A2199-M1
NGC 6173	BCG	126.2	2	–23.59	4.47	3	A2197-M1
NGC 6278	S0	40.0	2	–20.81	...	2	
NGC 6340	S0	16.8	2	–19.46	...	6	$\Delta M = 0.82$ (1)
NGC 6849	S0	84.0	4	–22.78	4.07	1	
NGC 6876	E	57.6	4	–23.58	...	1	
NGC 7014	BCG	71.1	2	–22.18	3.83	3	A3742-M1
NGC 7052	E	67.1	2	–22.35	4.12	5	
NGC 7213	Sa	22.7	3	–21.71	...	1	
NGC 7332	S0	24.3	1	–19.62	3.20	4	$\Delta M = 1.32$ (1)
NGC 7457	S0–	14.0	1	–18.62	3.83	1	$\Delta M = 1.08$ (3)
NGC 7578B	BCG	171.9	2	–23.41	4.57	3	A2572-M1
NGC 7619	E	56.1	1	–22.94	3.97	1	
NGC 7626	E	56.0	1	–22.87	4.08	5	
NGC 7647	BCG	171.4	2	–23.97	...	3	A2589-M1
NGC 7727	Sa	21.6	3	–21.19	...	1	
NGC 7743	S0+	21.9	1	–20.18	...	6	$\Delta M = 0.27$ (1)
NGC 7785	E	49.9	4	–22.08	3.62	1	
IC 0115	BCG	171.7	2	–22.67	4.19	3	A0195-M1
IC 0613	BCG	128.9	2	–22.27	4.32	3	A1016-M1
IC 0664	BCG	138.9	2	–22.86	4.37	3	A1142-M1
IC 0712	BCG	140.7	2	–23.29	4.85	3	A1314-M1
IC 0875	S0	41.9	2	–20.21	...	2	
IC 1459	E	30.9	1	–22.51	3.65	1	
IC 1565	BCG	38.2	2	–22.99	3.75	3	A0076-M1
IC 1633	BCG	98.4	2	–23.91	4.31	3	A2877-M1

Table 1—Continued

Galaxy	Morph	D (Mpc)	Ref	M_V	R_e log(pc)	S	Notes
IC 1695	BCG	192.0	2	−23.90	4.74	3	A0193-M1
IC 1733	BCG	150.4	2	−23.43	4.59	3	A0260-M1
IC 2738	BCG	152.7	2	−22.18	4.26	3	A1228-M1
IC 4329	BCG	56.7	4	−23.95	4.62	1	A3574-M1
IC 4931	BCG	83.3	2	−23.47	4.53	3	A3656-M1
IC 5353	BCG	124.0	2	−22.64	4.18	3	A4038-M1
A0119-M1	BCG	177.9	2	−24.01	4.66	3	
A0168-M1	BCG	177.9	2	−23.12	4.50	3	
A0189-M1	BCG	133.4	2	−21.89	3.97	3	
A0261-M1	BCG	181.6	2	−22.95	4.36	3	
A0295-M1	BCG	168.1	2	−23.11	4.60	3	
A0376-M1	BCG	195.2	2	−23.60	4.68	3	
A0397-M1	BCG	132.9	2	−23.42	4.53	3	
A0419-M1	BCG	156.0	2	−21.79	3.91	3	
A0496-M1	BCG	126.9	2	−24.28	4.77	3	
A0533-M1	BCG	179.4	2	−22.68	4.33	3	
A0548-M1	BCG	152.6	2	−22.75	4.32	3	
A0634-M1	BCG	117.3	2	−22.70	4.22	3	
A0912-M1	BCG	176.0	2	−22.24	3.98	3	
A0999-M1	BCG	128.9	2	−22.45	4.14	3	
A1020-M1	BCG	278.6	2	−22.65	...	4	
A1631-M1	BCG	176.7	2	−23.34	4.51	3	
A1831-M1	BCG	321.0	2	−23.51	...	4	
A1983-M1	BCG	176.1	2	−22.35	3.87	3	
A2040-M1	BCG	176.6	2	−23.46	4.71	3	
A2052-M1	BCG	150.9	2	−23.04	5.02	4	
A2147-M1	BCG	140.0	2	−23.16	4.56	3	
A2247-M1	BCG	163.3	2	−22.66	4.17	3	
A3144-M1	BCG	173.0	2	−22.28	4.04	3	
A3376-M1	BCG	176.0	2	−23.29	4.55	3	
A3395-M1	BCG	186.1	2	−24.23	4.91	3	
A3528-M1	BCG	204.6	2	−24.30	5.02	3	

Table 1—Continued

Galaxy	Morph	D (Mpc)	Ref	M_V	R_e log(pc)	S	Notes
A3532-M1	BCG	208.6	2	−24.58	5.06	3	
A3554-M1	BCG	180.9	2	−23.99	4.72	3	
A3556-M1	BCG	183.0	2	−23.65	4.30	3	
A3558-M1	BCG	180.8	2	−24.92	4.91	3	
A3562-M1	BCG	185.6	2	−24.32	5.11	3	
A3564-M1	BCG	186.2	2	−22.68	3.75	3	
A3570-M1	BCG	142.3	2	−22.54	4.37	3	
A3571-M1	BCG	151.3	2	−25.30	5.33	3	
A3677-M1	BCG	186.6	2	−22.21	4.42	3	
A3716-M1	BCG	180.2	2	−23.75	4.73	3	
A3736-M1	BCG	196.2	2	−23.98	4.62	3	
A3747-M1	BCG	128.6	2	−22.65	4.16	3	
ESO 378-20	S0	47.7	2	−20.97	...	2	
ESO 443-39	S0	47.2	2	−20.93	...	2	
ESO 447-30	S0	41.7	2	−21.17	...	2	
ESO 462-15	E	80.3	4	−22.83	3.86	1	
ESO 507-27	S0	50.1	2	−20.89	...	2	
ESO 507-45	S0	73.3	4	−23.28	...	5	
MCG 11-14-25A	E	49.0	2	−19.08	...	2	
MCG 8-27-18	S0	48.7	2	−20.03	...	2	
UGC 4551	S0	27.1	2	−19.78	...	2	
UGC 4587	S0	45.9	2	−20.77	...	2	
UGC 6062	S0	42.2	2	−20.34	...	2	
VCC 1199	E	17.9	1	−15.58	...	4	
VCC 1440	E	17.9	1	−17.24	...	4	
VCC 1545	E	17.9	1	−17.49	...	4	
VCC 1627	E	17.9	1	−16.42	...	4	

Note. — Morphological classifications are from the RC3 (de Vaucouleurs et al. 1991). Distance reference codes: 1) Tonry et al. (2001) SBF distances adjusted to $H_0 = 70 \text{ km s}^{-1} \text{ Mpc}^{-1}$; 2) distance from Faber et al. (1997)

scaled to $H_0 = 70$; 3) Faber et al. (1989) group distance; and 4) distance based on CMB velocity of galaxy or group. Galaxy absolute luminosities are based on RC3 V_T values, or the Laine et al. (2002) R magnitudes for the BGC; Schlegel et al. (1998) extinction corrections have been applied. The (S) column refers to the source of central structural parameters for the given galaxy as follows: 1) Lauer et al. (2005); 2) Rest et al. (2001); 3) Laine et al. (2002); 4) Lauer et al. (1995); 5) Quillen et al. (2000); and 6) Ravindranath et al. (2001). ΔM values in the notes column refer to the luminosity corrections applied to subtract the disks in S0 galaxies; reference codes in the parentheses correspond to 1) Baggett et al. (1998), 2) Baggett et al. (1998), 3) Kent (1985), 4) Kormendy & Illingworth (1983), 5) Boroson (1981), and 6) Burstein (1979).

Table 2. Central Structural Parameters

Galaxy	S	P	r_b (pc)	θ_b (arcsec)	I_b	α	β	γ	γ'	Notes
NGC 0404	6	\	1.7	0.40	16.01	0.0	1.58	0.28	0.92	\cap in ref. (6)
NGC 0474	6	\	14.2	1.47	17.17	1.2	1.90	0.37	0.56	\wedge in ref. (6)
NGC 0507	1	\cap	343.3	1.11	17.16	1.3	1.75	0.00	0.01	
NGC 0524	6	\cap	173.6	1.41	16.58	0.7	1.69	0.03	0.27	
NGC 0545	3	\cap	248.8	0.70	16.90	1.5	1.47	0.08	0.10	
NGC 0584	1	\cap	47.1	0.44	15.22	0.5	1.61	-0.01	0.30	
NGC 0596	1	\	4.3	0.54	15.90	0.5	1.59	0.16	0.54	
NGC 0720	4	\cap	487.0	3.44	17.45	2.2	1.43	0.06	0.07	
NGC 0741	1	\cap	391.9	1.14	17.67	2.3	1.29	0.10	0.11	
NGC 0821	1	\wedge	59.3	0.48	15.69	0.4	1.71	0.10	0.42	\ in ref. (6)
NGC 0910	3	\cap	153.3	0.39	16.93	4.2	0.91	-0.03	-0.03	
NGC 1016	1	\cap	618.2	1.68	18.01	1.0	1.90	0.09	0.11	
NGC 1023	1	\	2.3	1.23	15.71	7.2	1.15	0.74	0.74	
NGC 1052	5	\cap	43.7	0.44	14.62	2.2	1.27	0.18	0.22	
NGC 1172	4	\	4.4	0.54	16.66	0.3	2.21	-0.01	0.86	
NGC 1316	1	\wedge	79.2	0.72	14.86	2.3	1.14	0.35	0.35	\cap in ref. (4)
NGC 1331	5	\	11.7	2.91	19.32	3.4	1.29	0.57	0.57	
NGC 1351	5	\	10.2	1.00	16.26	3.8	1.31	0.78	0.78	
NGC 1374	1	\cap	9.1	0.09	14.57	1.9	1.08	-0.09	-0.03	
NGC 1399	1	\cap	239.4	2.34	16.96	2.3	1.32	0.12	0.12	
NGC 1400	4	\cap	39.8	0.31	15.43	1.2	1.35	-0.10	0.20	\ in ref. (5)
NGC 1426	1	\	5.1	2.20	17.62	0.5	1.96	0.26	0.57	
NGC 1427	1	\	4.1	0.86	16.25	0.8	1.67	0.30	0.51	
NGC 1439	1	\	5.1	0.65	16.21	4.8	1.48	0.74	0.74	
NGC 1500	3	\cap	167.0	0.26	16.70	1.4	1.37	0.08	0.20	
NGC 1553	5	\	10.2	5.72	16.93	3.8	1.43	0.74	0.74	
NGC 1600	4	\cap	1870.0	6.72	19.03	1.1	2.12	-0.03	0.00	
NGC 1700	1	\cap	11.8	0.06	13.58	1.0	1.19	-0.10	0.07	\ in ref. (4)
NGC 2300	1	\cap	330.1	2.24	17.53	1.2	1.80	0.07	0.08	
NGC 2434	1	\	4.4	5.41	19.10	1.9	2.05	0.75	0.75	
NGC 2549	2	\	3.2	3.70	17.57	1.8	1.71	0.67	0.67	
NGC 2592	2	\	6.6	1.37	17.22	3.3	1.60	0.92	0.92	

Table 2—Continued

Galaxy	S	P	r_b (pc)	θ_b (arcsec)	I_b	α	β	γ	γ'	Notes
NGC 2634	2	\	8.6	1.82	17.93	2.8	1.57	0.81	0.81	
NGC 2636	4	\	7.4	0.24	16.53	0.6	1.66	0.06	0.67	
NGC 2685	6	\	6.9	2.38	17.03	1.7	1.52	0.73	0.73	
NGC 2699	2	\	6.9	2.66	18.24	1.7	1.89	0.84	0.85	
NGC 2778	1	\	4.7	0.35	16.06	0.4	1.75	0.33	0.83	
NGC 2832	3	\cap	488.1	1.04	17.37	1.7	1.44	0.02	0.03	
NGC 2841	4	\wedge	11.7	0.16	14.52	1.6	0.92	0.05	0.34	\ in ref. (4)
NGC 2872	2	\	11.5	4.27	18.72	2.5	1.66	1.01	1.01	
NGC 2902	2	\wedge	140.8	0.88	16.95	1.9	1.57	0.49	0.50	\ in ref. (2)
NGC 2907	5	\	16.7	1.96	16.60	0.5	1.78	0.58	0.79	
NGC 2950	2	\	3.8	2.43	16.77	2.4	1.81	0.82	0.82	
NGC 2974	1	\	4.4	0.31	15.17	25.1	1.05	0.62	0.62	
NGC 2986	2	\cap	226.0	1.24	16.70	1.8	1.50	0.18	0.18	
NGC 3056	5	\	6.3	4.11	18.05	2.1	1.80	0.90	0.90	
NGC 3065	2	\	7.2	3.14	18.58	1.0	2.28	0.79	0.84	
NGC 3078	2	\	9.0	3.43	17.80	2.4	1.60	0.95	0.95	
NGC 3115	1	\	2.0	0.86	14.48	4.3	1.09	0.52	0.52	
NGC 3193	2	\cap	141.4	0.81	16.07	0.6	1.89	0.01	0.28	\wedge in ref. (2)
NGC 3266	2	\	7.1	2.25	18.39	1.3	2.06	0.64	0.66	
NGC 3348	2	\cap	199.2	0.99	16.61	1.2	1.53	0.09	0.12	
NGC 3377	1	\	2.3	0.31	14.12	0.3	1.96	0.03	0.62	
NGC 3379	1	\cap	112.3	1.98	16.15	1.5	1.54	0.18	0.18	
NGC 3384	1	\	2.3	3.15	16.44	15.3	1.81	0.71	0.71	
NGC 3414	2	\	6.5	1.72	17.07	1.4	1.45	0.83	0.84	
NGC 3551	3	\cap	359.5	0.57	17.64	1.8	1.31	0.13	0.14	
NGC 3585	1	\wedge	37.0	0.36	14.72	1.6	1.06	0.31	0.31	
NGC 3595	2	\	8.5	2.30	18.04	2.3	1.52	0.75	0.76	
NGC 3599	4	\	4.5	1.25	17.45	50.0	1.45	0.75	0.75	
NGC 3605	4	\	4.5	0.97	17.21	2.4	1.27	0.59	0.60	
NGC 3607	1	\cap	128.4	2.43	16.87	2.1	1.70	0.26	0.26	
NGC 3608	1	\cap	53.5	0.48	15.73	0.9	1.50	0.09	0.17	
NGC 3610	1	\	4.4	2.84	16.39	48.5	1.86	0.76	0.76	

Table 2—Continued

Galaxy	S	P	r_b (pc)	θ_b (arcsec)	I_b	α	β	γ	γ'	Notes
NGC 3613	2	\cap	50.8	0.34	15.72	1.5	1.06	0.04	0.08	
NGC 3640	1	\cap	46.6	0.34	15.66	0.6	1.30	-0.10	0.03	\wedge in ref. (2)
NGC 3706	1	\cap	40.9	0.18	14.18	14.7	1.24	-0.01	-0.01	
NGC 3842	3	\cap	399.9	0.93	17.60	2.2	1.27	0.11	0.12	
NGC 3900	6	\setminus	14.5	0.23	15.20	0.3	1.66	0.51	1.02	
NGC 3945	1	\setminus	3.9	7.38	18.62	0.3	2.56	-0.06	0.57	
NGC 4026	1	\setminus	3.0	0.63	15.23	0.4	1.78	0.15	0.65	
NGC 4073	1	\cap	129.6	0.29	16.53	4.4	0.99	-0.08	-0.08	
NGC 4121	2	\setminus	6.1	5.60	20.30	1.5	3.65	0.85	0.85	
NGC 4128	2	\setminus	8.4	1.59	16.92	1.1	1.69	0.71	0.75	
NGC 4143	6	\setminus	7.6	3.11	17.11	1.3	2.18	0.59	0.61	
NGC 4150	6	\setminus	8.4	0.63	15.80	1.2	1.67	0.58	0.68	
NGC 4168	2	\cap	365.3	2.02	18.06	1.4	1.39	0.17	0.17	
NGC 4239	2	\wedge	29.7	0.35	17.38	0.3	1.25	-0.06	0.46	
NGC 4261	6	\cap	262.3	1.62	16.43	2.4	1.43	0.00	0.00	
NGC 4278	1	\cap	102.0	1.26	16.20	1.4	1.46	0.06	0.10	
NGC 4291	1	\cap	72.7	0.60	15.66	1.5	1.60	0.01	0.02	
NGC 4365	1	\cap	231.4	2.21	16.88	1.7	1.52	0.07	0.09	
NGC 4374	6	\cap	207.4	2.39	16.20	2.1	1.50	0.13	0.13	
NGC 4382	1	\cap	80.7	0.93	15.67	1.1	1.39	0.00	0.01	
NGC 4387	4	\setminus	3.5	0.44	16.85	0.2	1.37	0.10	0.65	
NGC 4406	1	\cap	79.8	0.92	16.03	3.9	1.04	-0.04	-0.04	
NGC 4417	6	\setminus	8.7	3.66	17.59	0.9	1.77	0.71	0.75	
NGC 4434	4	\setminus	3.5	0.61	16.57	0.4	1.97	-0.04	0.64	
NGC 4458	1	\cap	7.8	0.09	13.72	4.5	1.40	0.16	0.17	\setminus in ref. (4)
NGC 4464	4	\setminus	3.5	0.60	16.23	0.5	1.99	0.14	0.70	
NGC 4467	4	\setminus	3.5	10.72	22.91	2.2	7.14	0.94	0.94	
NGC 4472	1	\cap	211.7	2.44	16.63	1.9	1.17	0.01	0.01	
NGC 4473	1	\cap	386.2	4.45	17.24	0.7	2.60	-0.07	0.01	
NGC 4474	2	\setminus	5.2	4.55	18.58	2.3	1.65	0.72	0.72	
NGC 4478	1	\cap	19.1	0.22	15.46	1.9	1.01	-0.10	0.10	\setminus in ref. (4)
NGC 4482	2	\wedge	350.6	4.04	20.24	3.4	1.01	0.49	0.49	\setminus in ref. (2)

Table 2—Continued

Galaxy	S	P	r_b (pc)	θ_b (arcsec)	I_b	α	β	γ	γ'	Notes
NGC 4486	4	\cap	491.2	5.66	17.32	8.4	1.06	0.27	0.27	
NGC 4486B	1	\cap	13.9	0.16	14.53	2.8	1.39	-0.10	-0.10	
NGC 4494	1	\backslash	3.5	2.82	17.19	0.7	1.88	0.52	0.55	
NGC 4503	2	\backslash	4.3	1.65	17.14	1.8	1.30	0.64	0.65	
NGC 4551	4	\backslash	3.5	0.34	16.49	0.2	1.64	-0.07	0.69	
NGC 4552	1	\cap	42.5	0.49	15.20	2.0	1.17	-0.10	-0.02	
NGC 4564	2	\backslash	4.3	1.28	16.50	1.4	1.27	0.80	0.81	
NGC 4589	1	\cap	67.9	0.56	16.08	1.1	1.32	0.21	0.25	\wedge in ref. (2)
NGC 4621	1	\backslash	3.5	1.00	15.76	0.4	1.34	0.75	0.85	
NGC 4636	6	\cap	298.5	3.44	17.45	1.7	1.56	0.13	0.13	
NGC 4648	2	\backslash	6.7	1.02	16.48	3.7	1.54	0.92	0.92	
NGC 4649	1	\cap	388.8	4.48	17.17	1.9	1.46	0.17	0.17	
NGC 4660	1	\backslash	3.5	1.76	16.34	5.6	1.50	0.91	0.91	
NGC 4696	3	\cap	271.5	1.40	17.76	6.6	0.86	0.10	0.10	
NGC 4697	4	\backslash	2.6	1.49	16.34	0.4	1.25	0.22	0.51	
NGC 4709	1	\wedge	227.8	1.27	17.48	2.2	1.43	0.32	0.32	
NGC 4742	4	\backslash	3.2	2.00	16.86	50.0	2.13	1.04	1.04	
NGC 4874	4	\cap	1731.3	3.35	19.40	1.9	1.61	0.12	0.12	
NGC 4889	3	\cap	967.2	2.10	18.03	2.1	1.46	0.03	0.03	
NGC 5017	2	\backslash	9.8	1.48	17.53	3.0	1.59	1.12	1.12	
NGC 5061	1	\cap	37.8	0.29	14.35	1.6	1.43	0.04	0.05	
NGC 5077	2	\cap	350.5	1.61	17.10	1.1	1.67	0.23	0.26	\wedge in ref. (2)
NGC 5198	2	\cap	29.7	0.16	15.40	2.6	1.13	0.23	0.26	\wedge in ref. (2)
NGC 5308	2	\backslash	8.0	0.83	16.16	0.4	1.27	0.82	0.96	
NGC 5370	2	\backslash	11.0	1.63	18.45	0.8	1.50	0.62	0.67	
NGC 5419	1	\cap	722.3	2.38	17.87	1.4	1.69	-0.10	0.03	
NGC 5557	1	\cap	204.4	0.80	16.40	0.8	1.68	0.02	0.07	\wedge in ref. (2)
NGC 5576	1	\cap	549.2	4.18	17.81	0.4	2.73	0.01	0.26	\backslash in ref. (2)
NGC 5796	2	\wedge	232.3	1.06	16.80	0.8	1.67	0.41	0.49	\backslash in ref. (2)
NGC 5812	2	\backslash	6.9	1.84	17.22	1.2	1.67	0.59	0.62	
NGC 5813	1	\cap	160.0	1.15	16.82	1.6	1.60	0.05	0.06	
NGC 5831	2	\backslash	7.0	1.78	17.51	0.5	1.84	0.33	0.55	

Table 2—Continued

Galaxy	S	P	r_b (pc)	θ_b (arcsec)	I_b	α	β	γ	γ'	Notes
NGC 5838	6	\	10.8	4.35	17.69	2.6	1.87	0.93	0.93	
NGC 5845	5	\	13.9	1.38	15.86	2.1	2.18	0.51	0.52	
NGC 5898	2	^	200.2	1.24	16.93	1.2	1.57	0.41	0.43	\ in ref. (2)
NGC 5903	2	∩	256.7	1.59	17.45	1.8	1.48	0.13	0.13	
NGC 5982	1	∩	68.7	0.35	15.66	2.1	1.03	0.05	0.05	
NGC 6086	3	∩	661.5	1.04	17.75	1.4	1.78	−0.01	0.02	
NGC 6166	4	∩	1502.6	2.41	19.33	4.3	0.91	0.12	0.12	
NGC 6173	3	∩	477.2	0.78	17.28	0.6	1.86	−0.33	0.02	
NGC 6278	2	\	9.7	0.60	16.30	0.8	1.62	0.55	0.67	
NGC 6340	6	\	8.1	0.28	15.39	2.5	1.28	0.59	0.64	
NGC 6849	1	∩	138.5	0.34	17.03	1.0	1.21	0.01	0.08	
NGC 6876	1	∩	139.6	0.50	16.99	12.1	0.75	0.00	0.00	
NGC 7014	3	∩	75.8	0.22	15.61	2.2	1.05	0.08	0.11	
NGC 7052	5	∩	250.5	0.77	16.35	2.8	1.19	0.16	0.16	
NGC 7213	1	∩	383.0	3.48	17.71	1.0	3.10	0.06	0.21	
NGC 7332	4	\	4.7	1.01	15.91	0.6	1.59	0.62	0.80	
NGC 7457	1	\	2.7	0.22	16.33	1.0	1.05	−0.10	0.61	^ in ref. (6)
NGC 7578B	3	∩	150.0	0.18	16.35	1.7	1.12	0.10	0.21	
NGC 7619	1	∩	223.0	0.82	16.41	1.1	1.63	−0.02	0.01	
NGC 7626	6	^	160.2	0.59	16.09	1.8	1.30	0.36	0.40	\ in ref. (5)
NGC 7647	3	∩	207.7	0.25	17.19	3.4	1.10	0.04	0.05	
NGC 7727	1	^	601.1	5.74	18.42	0.6	1.93	0.43	0.49	
NGC 7743	6	\	10.6	0.16	14.44	5.4	1.38	0.50	0.57	
NGC 7785	1	∩	16.9	0.07	15.14	0.9	0.97	−0.10	0.06	
IC 0115	3	∩	407.9	0.49	17.49	2.1	1.41	0.09	0.10	
IC 0613	3	∩	143.7	0.23	16.41	3.9	1.16	0.24	0.25	
IC 0664	3	∩	127.9	0.19	15.86	9.3	1.31	0.12	0.12	
IC 0712	3	∩	811.7	1.19	18.06	2.3	1.60	0.17	0.17	
IC 0875	2	\	10.2	1.87	18.26	0.8	1.81	1.07	1.12	
IC 1459	1	∩	293.6	1.96	16.36	0.8	2.08	−0.10	0.15	
IC 1565	3	∩	51.9	0.28	16.94	1.2	1.33	−0.20	−0.03	
IC 1633	3	∩	467.5	0.98	17.04	1.3	1.58	−0.02	0.01	

Table 2—Continued

Galaxy	S	P	r_b (pc)	θ_b (arcsec)	I_b	α	β	γ	γ'	Notes
IC 1695	3	∩	363.0	0.39	17.01	2.8	1.48	0.23	0.23	
IC 1733	3	∩	546.9	0.75	17.71	3.4	1.29	−0.01	−0.01	
IC 2738	3	\	37.0	0.08	16.61	1.4	1.41	0.53	0.60	
IC 4329	3	∩	208.9	0.76	16.97	2.5	1.30	−0.02	−0.02	
IC 4931	3	∩	399.8	0.99	17.14	2.1	1.46	0.09	0.09	
IC 5353	3	∩	198.4	0.33	16.77	1.2	1.44	0.03	0.17	
A0119-M1	3	∩	690.0	0.80	18.56	3.1	1.06	0.06	0.06	
A0168-M1	3	∩	51.7	0.06	16.62	0.9	1.02	−0.48	0.19	
A0189-M1	3	\	32.3	0.05	17.56	9.8	1.22	0.85	0.85	
A0261-M1	3	\	44.0	0.05	18.22	10.0	1.47	0.76	0.76	
A0295-M1	3	∩	513.4	0.63	17.93	3.8	1.24	0.13	0.13	
A0376-M1	3	∩	643.5	0.68	18.36	2.4	1.28	0.19	0.20	
A0397-M1	3	∩	683.0	1.06	18.02	2.7	1.50	0.07	0.07	
A0419-M1	3	\	37.8	0.10	17.77	0.6	1.64	0.33	0.60	
A0496-M1	3	∩	449.1	0.73	18.20	2.2	1.01	0.10	0.10	
A0533-M1	3	∩	269.6	0.31	17.30	1.8	1.31	0.06	0.10	
A0548-M1	3	∩	295.9	0.40	17.50	1.0	1.38	0.00	0.16	
A0634-M1	3	∩	130.8	0.23	17.10	3.0	0.88	−0.05	−0.04	
A0912-M1	3	\	42.7	0.08	16.78	1.7	1.34	0.48	0.55	
A0999-M1	3	∩	387.5	0.62	17.50	1.1	1.65	−0.06	0.05	
A1020-M1	4	∩	283.6	0.21	17.06	1.7	1.47	−0.09	0.25	
A1631-M1	3	∩	171.3	0.20	16.65	1.5	1.29	−0.03	0.12	
A1831-M1	4	∩	762.6	0.49	18.63	5.3	1.11	0.12	0.12	
A1983-M1	3	∧	85.4	0.10	15.79	0.3	2.63	−1.37	0.44	
A2040-M1	3	∩	333.9	0.39	17.80	1.7	1.39	0.16	0.19	
A2052-M1	4	∩	234.1	0.32	18.44	4.5	0.73	−0.08	0.01	
A2052-M1	4	∩	234.1	0.32	18.44	4.5	0.73	−0.08	0.01	
A2147-M1	3	∩	1500.0	2.21	19.47	1.6	1.37	0.18	0.18	
A2247-M1	3	\	39.6	0.03	19.39	1.9	1.42	0.85	0.85	
A3144-M1	3	∩	327.1	0.39	17.19	1.8	1.64	0.07	0.11	
A3376-M1	3	∩	1663.9	1.95	19.10	3.1	1.50	0.05	0.05	
A3395-M1	3	∩	333.8	0.37	18.09	2.4	0.98	0.03	0.04	

Table 2—Continued

Galaxy	S	P	r_b (pc)	θ_b (arcsec)	I_b	α	β	γ	γ'	Notes
A3528-M1	3	\cap	605.1	0.61	17.81	2.5	1.35	0.18	0.18	
A3532-M1	3	\cap	434.9	0.43	17.68	3.1	1.30	0.18	0.18	
A3554-M1	3	\cap	456.1	0.52	18.42	2.7	1.10	0.04	0.04	
A3556-M1	3	\cap	417.0	0.47	17.16	2.2	1.34	0.09	0.10	
A3558-M1	3	\cap	1516.4	1.73	19.37	2.1	1.10	0.05	0.05	
A3562-M1	3	\cap	1034.8	1.15	19.13	1.2	1.32	0.00	0.03	
A3564-M1	3	\cap	216.7	0.24	16.96	1.3	1.38	0.05	0.20	
A3570-M1	3	\cap	179.4	0.26	16.56	1.3	1.50	0.00	0.17	
A3571-M1	3	\cap	843.5	1.15	19.28	2.9	0.75	0.02	0.02	
A3677-M1	3	\cap	244.3	0.27	16.89	1.3	1.63	-0.04	0.13	
A3716-M1	3	\cap	384.4	0.44	18.02	2.4	1.10	-0.03	-0.02	
A3736-M1	3	\cap	875.1	0.92	18.29	1.4	1.33	0.11	0.13	
A3747-M1	3	\cap	112.2	0.18	16.04	2.1	1.16	-0.02	0.05	
ESO 378-20	2	\backslash	11.6	2.41	18.22	0.4	2.00	0.86	1.09	
ESO 443-39	2	\backslash	11.4	1.30	17.93	1.4	1.31	0.75	0.77	
ESO 447-30	2	\backslash	10.1	1.50	17.34	2.7	1.72	0.84	0.84	
ESO 462-15	1	\backslash	15.6	0.41	16.59	0.2	1.77	-0.10	0.56	
ESO 507-27	2	\backslash	12.1	3.89	18.57	0.6	1.58	0.70	0.79	
ESO 507-45	5	\wedge	117.3	0.33	15.34	1.3	1.26	0.16	0.35	\cap in ref. (5)
MCG 11-14-25A	2	\cap	133.0	0.56	17.20	0.7	2.13	0.00	0.30	\wedge in ref. (2)
MCG 08-27-18	2	\backslash	11.8	1.95	19.22	0.8	1.93	0.79	0.89	
UGC 04551	2	\backslash	6.6	2.26	17.67	2.2	2.16	0.51	0.51	
UGC 04587	2	\backslash	11.1	0.19	16.09	1.0	1.24	0.72	0.81	
UGC 06062	2	\backslash	10.2	2.75	18.96	0.9	1.81	0.80	0.82	
VCC 1199	4	\backslash	3.5	1.60	19.72	0.3	2.96	-0.08	0.90	
VCC 1440	4	\backslash	3.5	0.15	16.86	0.2	1.71	0.14	0.89	
VCC 1545	4	\backslash	3.5	2.50	20.43	0.3	1.78	0.05	0.51	
VCC 1627	4	\backslash	3.5	0.56	17.89	0.4	2.22	-0.10	0.69	

Note. — The profile type, P, is \backslash = power-law, \wedge = intermediate form, and \cap = core. The source column refers to the origin of central structural parameters for the given galaxy as follows: 1) Lauer et al. (2005); 2) Rest et al. (2001); 3) Laine et al. (2002); 4) Lauer et al. (1995) or Faber et al. (1997); 5) Quillen et al. (2000); and 6) Ravindranath et al. (2001). The notes column gives previous profile classifications and their source if different from the present classification.

Table 3. Bimodal Distributions of γ'

Sample	N	f_1	f_2	$\bar{\gamma}'_1$	$\bar{\gamma}'_2$	σ_1	σ_2	$P_1(0.95)$	$P_1 = P_2$	$P_2(0.95)$
Full Sample	223	0.576	0.424	0.13	0.73	0.14	0.14	0.23	0.44	0.52
Full Sample	223	0.535	0.465	0.11	0.69	0.09	0.19	0.23	0.31	0.37
$D \leq 50$ Mpc	144	0.413	0.587	0.16	0.73	0.16	0.16	0.30	0.43	0.55
$D \leq 50$ Mpc	144	0.377	0.623	0.13	0.72	0.11	0.18	0.24	0.33	0.43
$M_V = -21.5 \pm 1.0$	97	0.585	0.415	0.17	0.73	0.16	0.16	0.31	0.49	0.57
$M_V = -21.5 \pm 1.0$	97	0.472	0.528	0.12	0.65	0.10	0.24	0.16	0.32	0.43

Note. — For each sample listed, the distribution of γ' is parameterized as the sum of two gaussian distributions. The “1” subscript refers to the gaussian describing the nominal core galaxies, while “2” corresponds to the power-law galaxies. The fraction of the sample in each is given by f_1 and f_2 , the sample means are $\bar{\gamma}'_1$ and $\bar{\gamma}'_2$, and the dispersions are σ_1 and σ_2 . Note that in the first distribution listed for each sample both dispersions are constrained to have the same value. The last three columns give the γ' values at which the probability of being in the core populations is 95%, the probabilities of being in either population are equal, and the probability of being a power-law galaxy is 95%.

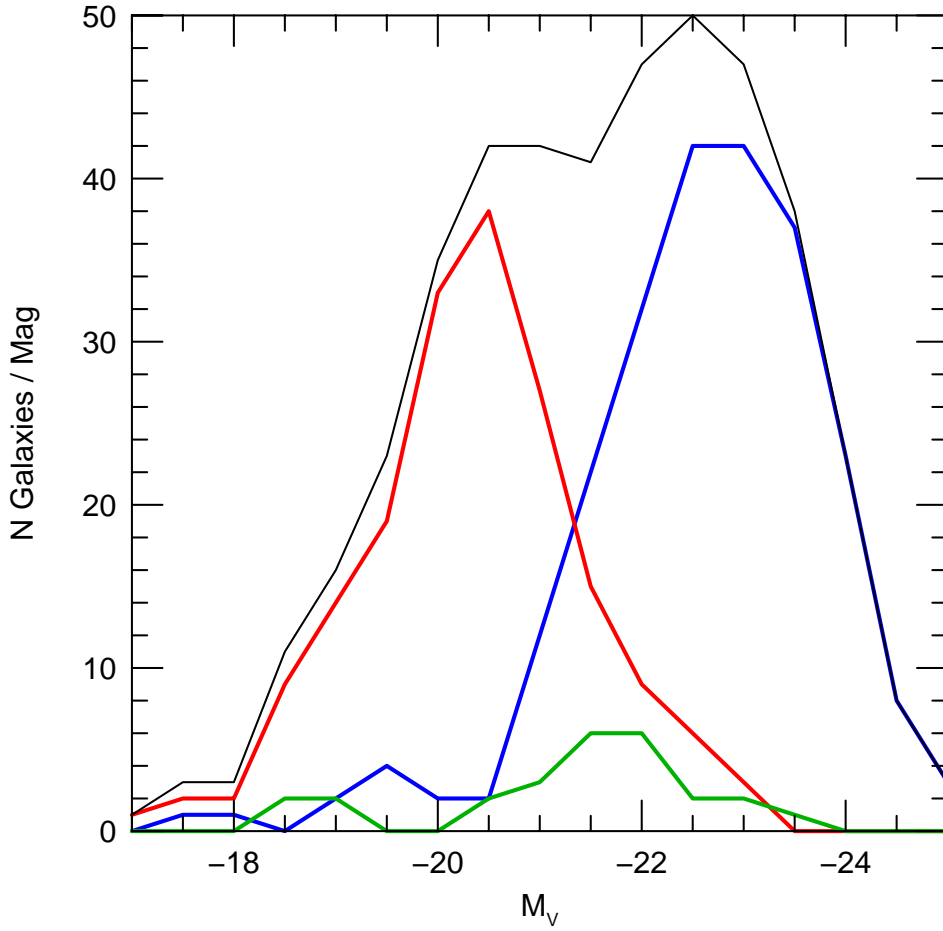


Fig. 1.— Histograms are plotted showing the frequency of core galaxies (blue line), power-law galaxies (red line), and intermediate galaxies (green line) as a function of luminosity in our sample of 219 galaxies. The thin line shows the total distribution of galaxies with luminosity. Note that the low-luminosity end of the power-law galaxy distribution and the high-luminosity end of the core galaxy distribution are likely to reflect biases with luminosity in the construction of the sample, but there are no obvious biases that affect the luminosity range $-22.5 \leq M_V \leq -20.5$ over which the frequency of power-law galaxies decreases as that of the core galaxies increases.

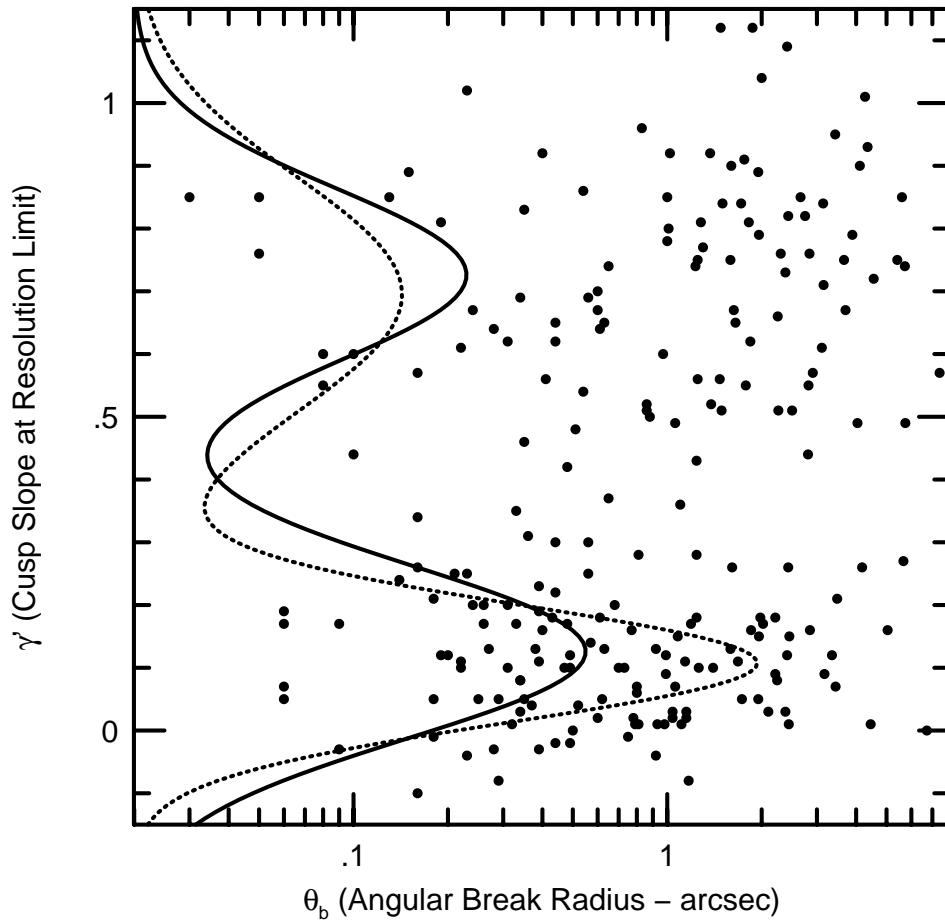


Fig. 2.— The limiting logarithmic slope γ' of the surface photometry profiles of the sample is plotted as a function of the angular size of the break radius. The solid line shows the distribution of γ' modeled as the sum of two gaussians with equal dispersions. The dashed line shows the distribution when the two gaussians are allowed to have differing dispersions. The normalization is arbitrary, but is the same for both distributions.

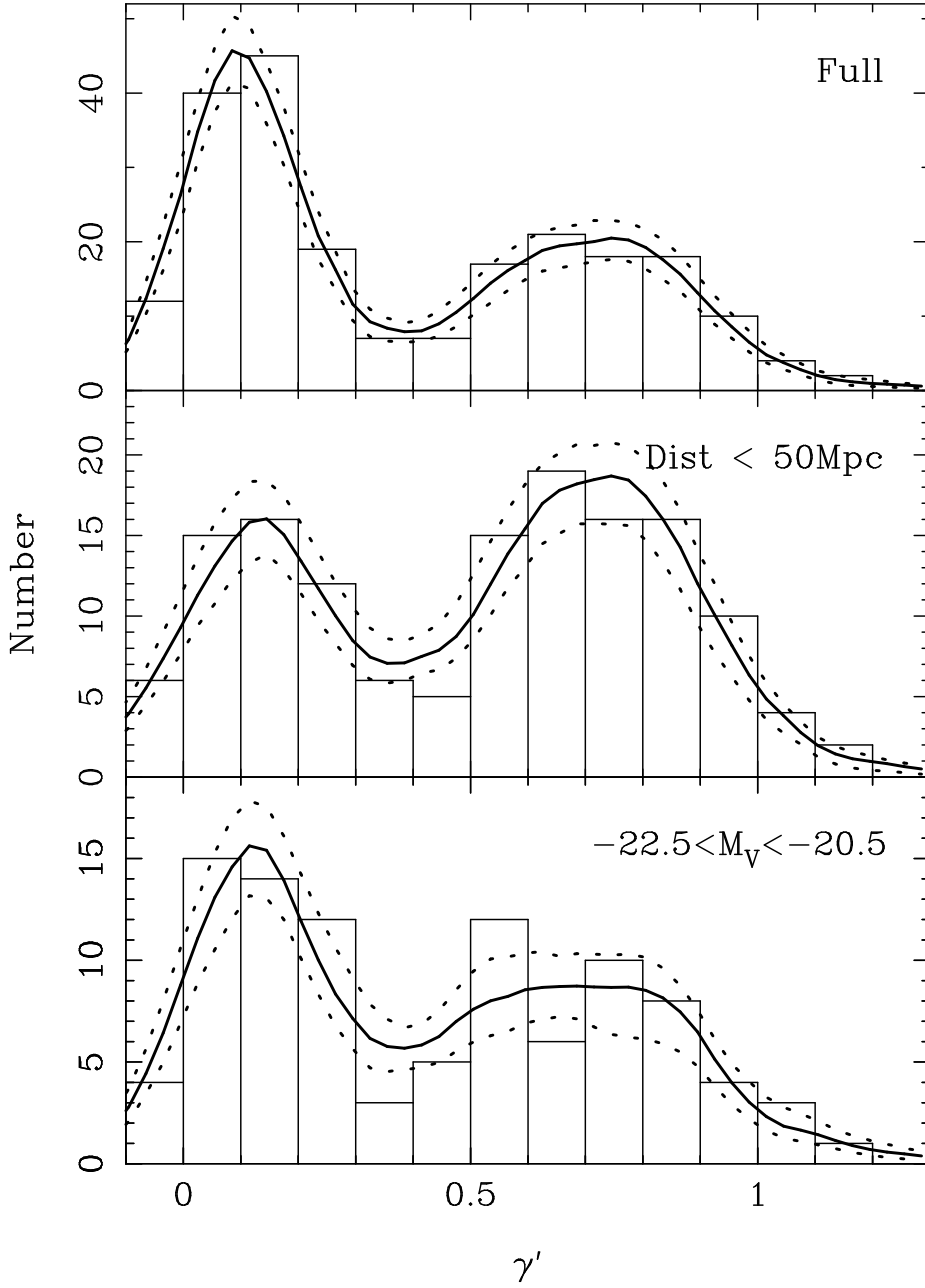


Fig. 3.— Histograms smoothed with an adaptive kernel are shown for three representations of the sample distribution of γ' . The top panel shows the histogram derived from the entire sample, the second panel just shows galaxies within 50 Mpc, and the bottom panel just has galaxies with $-22.5 \leq M_V \leq -20.5$. The dashed lines show the 1σ confidence intervals. The bimodality of all three histograms is highly significant.

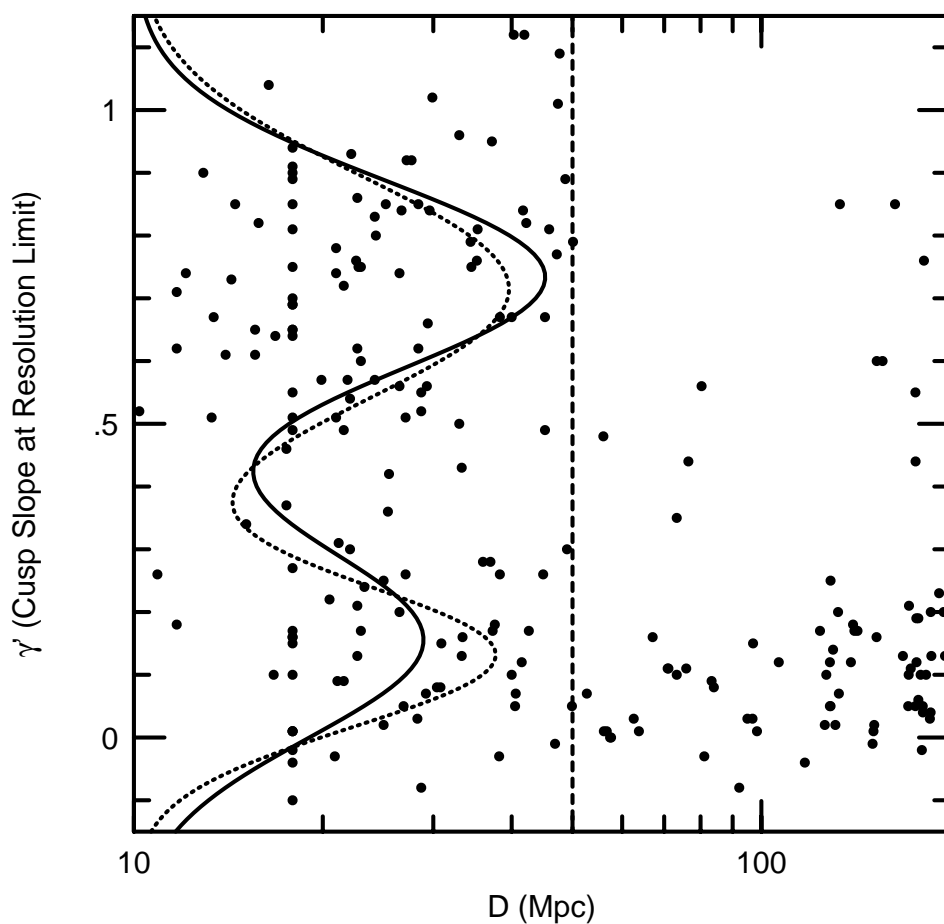


Fig. 4.— The limiting logarithmic slope γ' of the surface photometry profiles of the sample is plotted as a function of distance. The solid line shows the distribution of γ' for just those galaxies with $D \leq 50$ Mpc (vertical line) modeled as the sum of two gaussians with equal dispersions. The dashed line shows the distribution when the two gaussians are allowed to have differing dispersions. The normalization is arbitrary but is the same for both distributions.

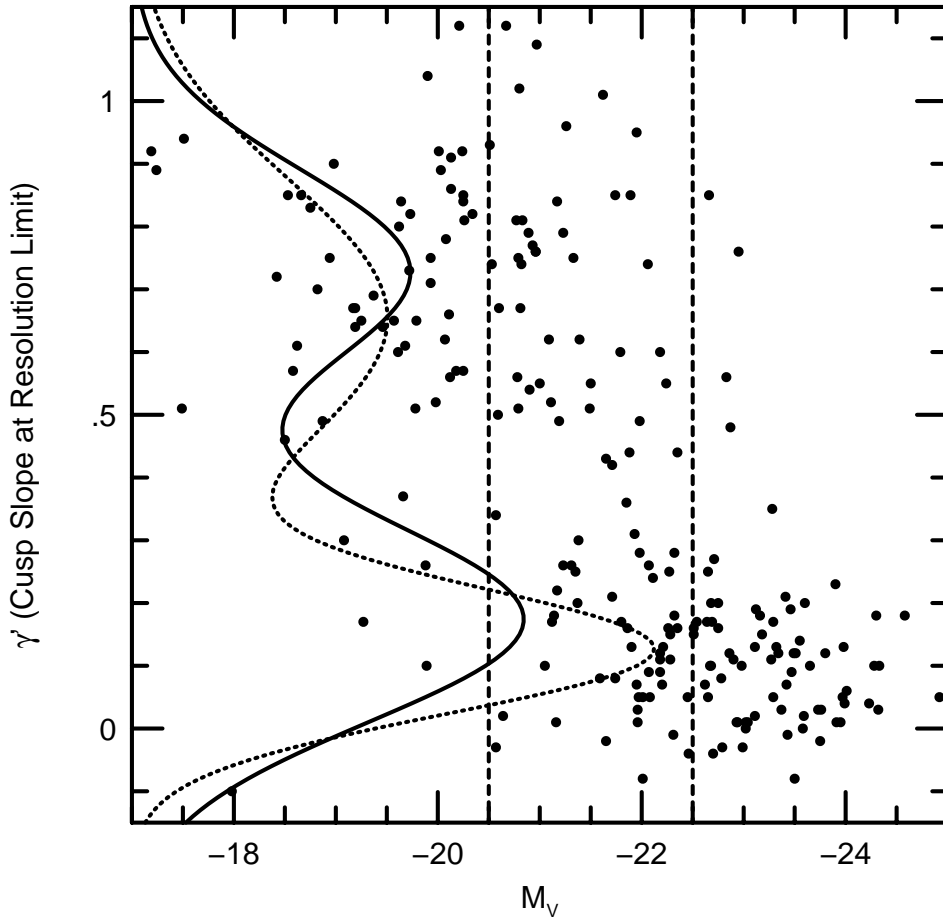


Fig. 5.— The limiting logarithmic-slope γ' of the surface photometry profiles of the sample is plotted as a function of galaxy luminosity. The solid line shows the distribution of γ' for just those galaxies with $-20.5 \geq M_V > -22.5$ (double vertical lines) modeled as the sum of two Gaussians with equal dispersions. The dashed line shows the distribution when the two Gaussians are allowed to have differing dispersions. The normalization is arbitrary but is the same for both distributions.

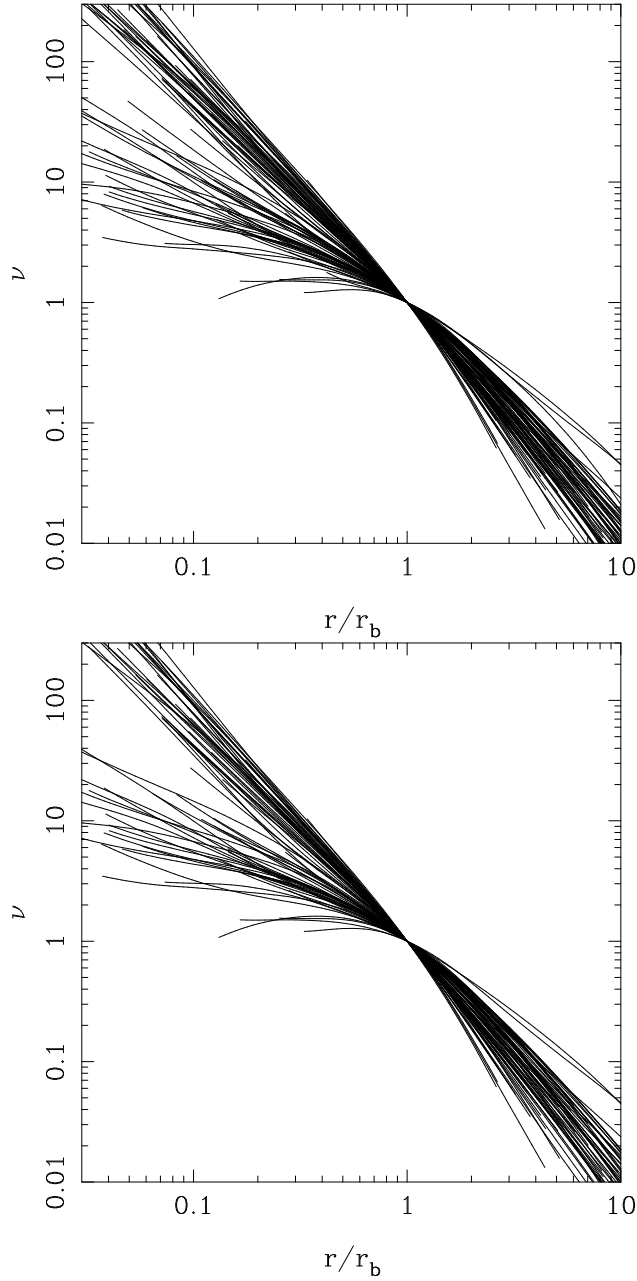


Fig. 6.— Luminosity density profiles are shown for the subset of galaxies for which WFC2 brightness profiles are available (as opposed to galaxies for which we have only the Nuker-law parameters). The Laine et al. (2002) BCG sample is also excluded. The radial scale is normalized by Nuker law break-radius, but the real measured brightness profiles were used rather than the Nuker-law fits. The slopes of the profiles for $r < r_b$ are strongly bimodal. The lower graph excludes galaxies in Lauer et al. (2005) with dust strength greater than 1.0.

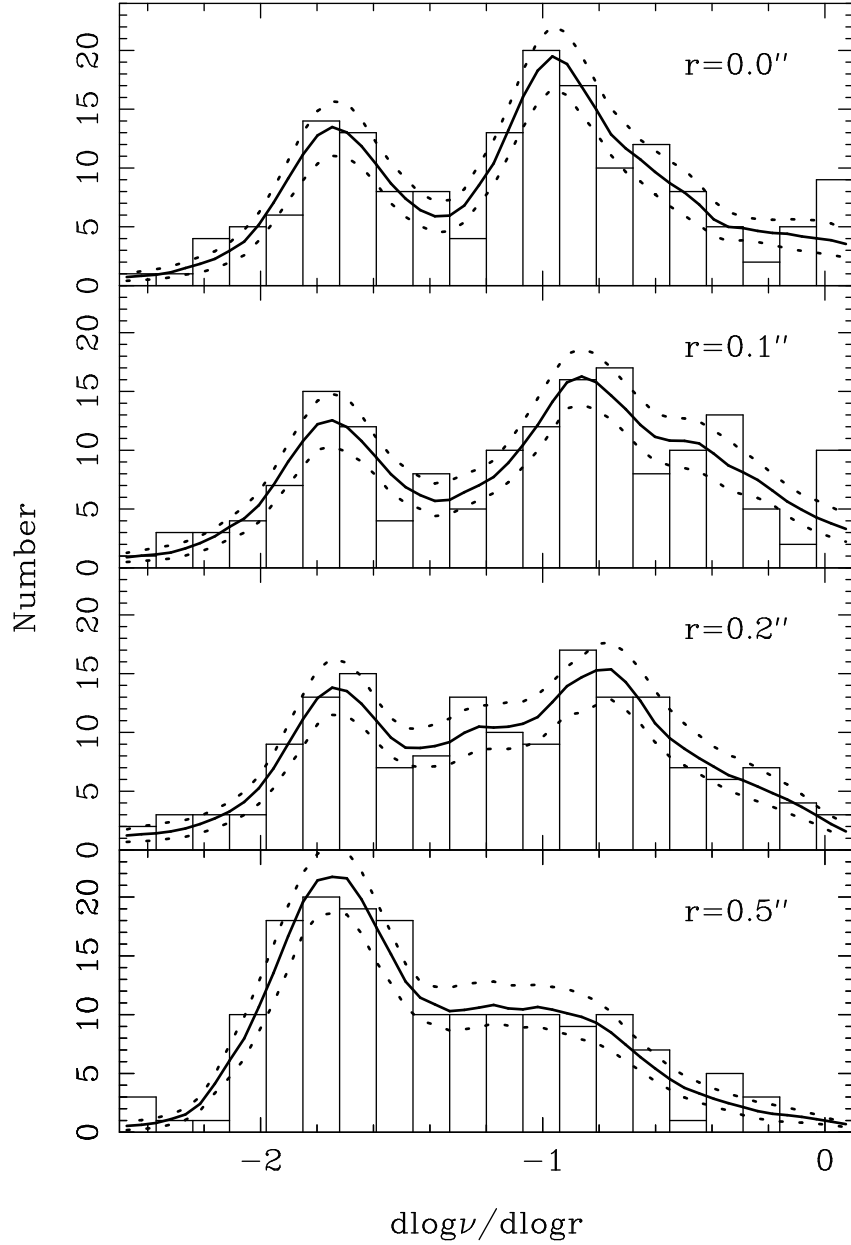


Fig. 7.— Histograms of the limiting slope of the luminosity density profiles are shown for various limiting radii. The bimodality of the histograms with the limiting $r \leq 0''.1$ is highly significant.

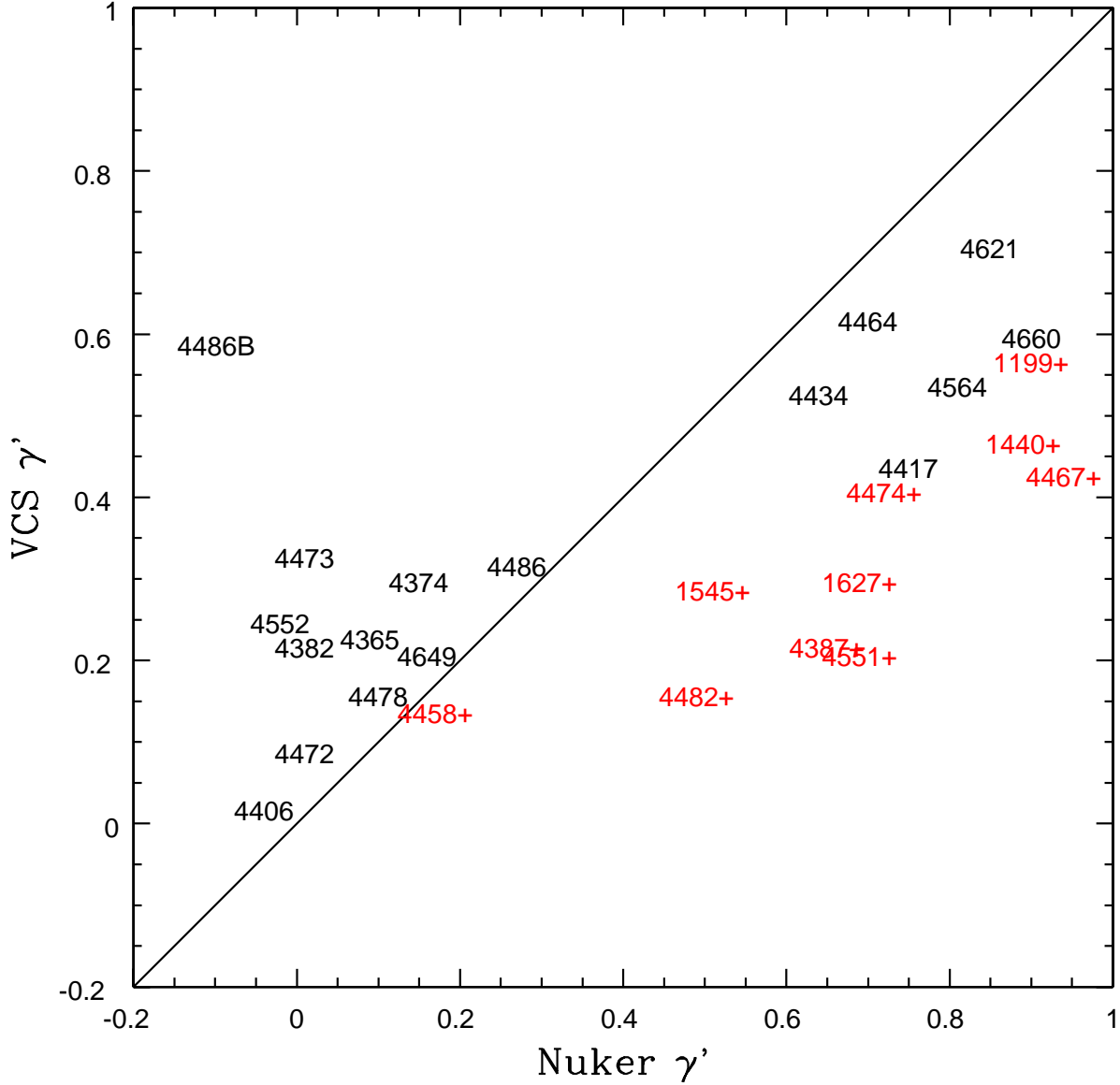


Fig. 8.— The limiting logarithmic slope γ' of the galaxy brightness profiles as the *HST* resolution limit is approached is plotted for 27 galaxies in common between the present and Ferrarese et al. (2006) VCS samples. The horizontal axis gives γ' estimated from Nuker law fits. The limiting resolution is typically between $0''.04$ and $0''.1$, depending on the source material. The vertical axis gives γ' estimated at $r = 0''.1$ from the VCS Sérsic or Core-Sérsic models. Galaxies plotted in red and marked with “+” are systems in which Ferrarese et al. (2006) fitted a Sérsic model plus a central nuclear component.

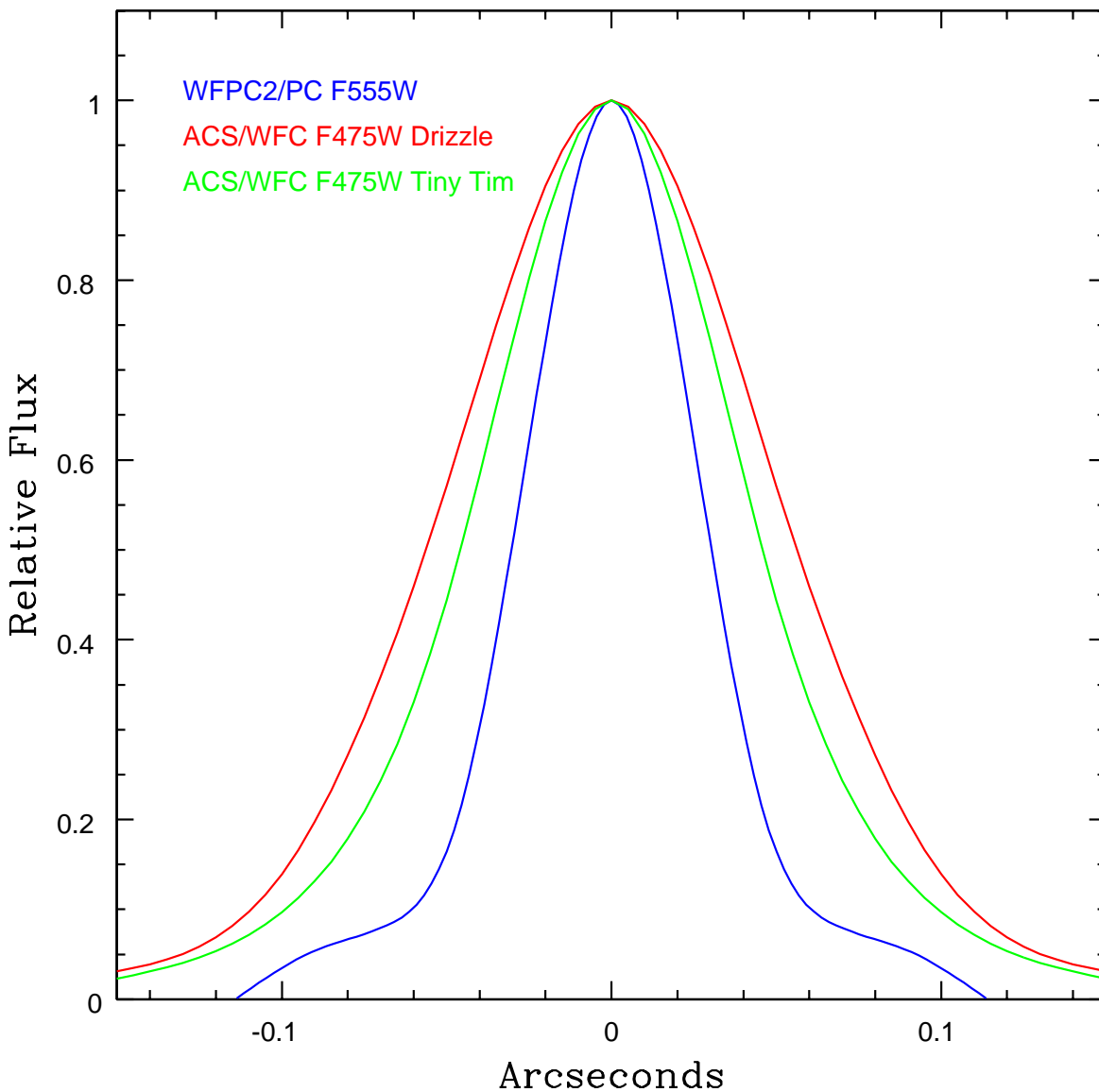


Fig. 9.— The widths of the WFPC2/PC F555W (blue) and ACS/WFC F475W PSFs (green and red) are compared. The highest resolution material in the present sample uses the former filter/instrument combination, while the Ferrarese et al. (2006) VCS program uses the latter. The two traces for the ACS PSF are from the *Tiny Tim* calculated PSF (green), and from a star in a “drizzled” image (red), which slightly degrades the native PSF. The WFPC2 PSF is significantly sharper.

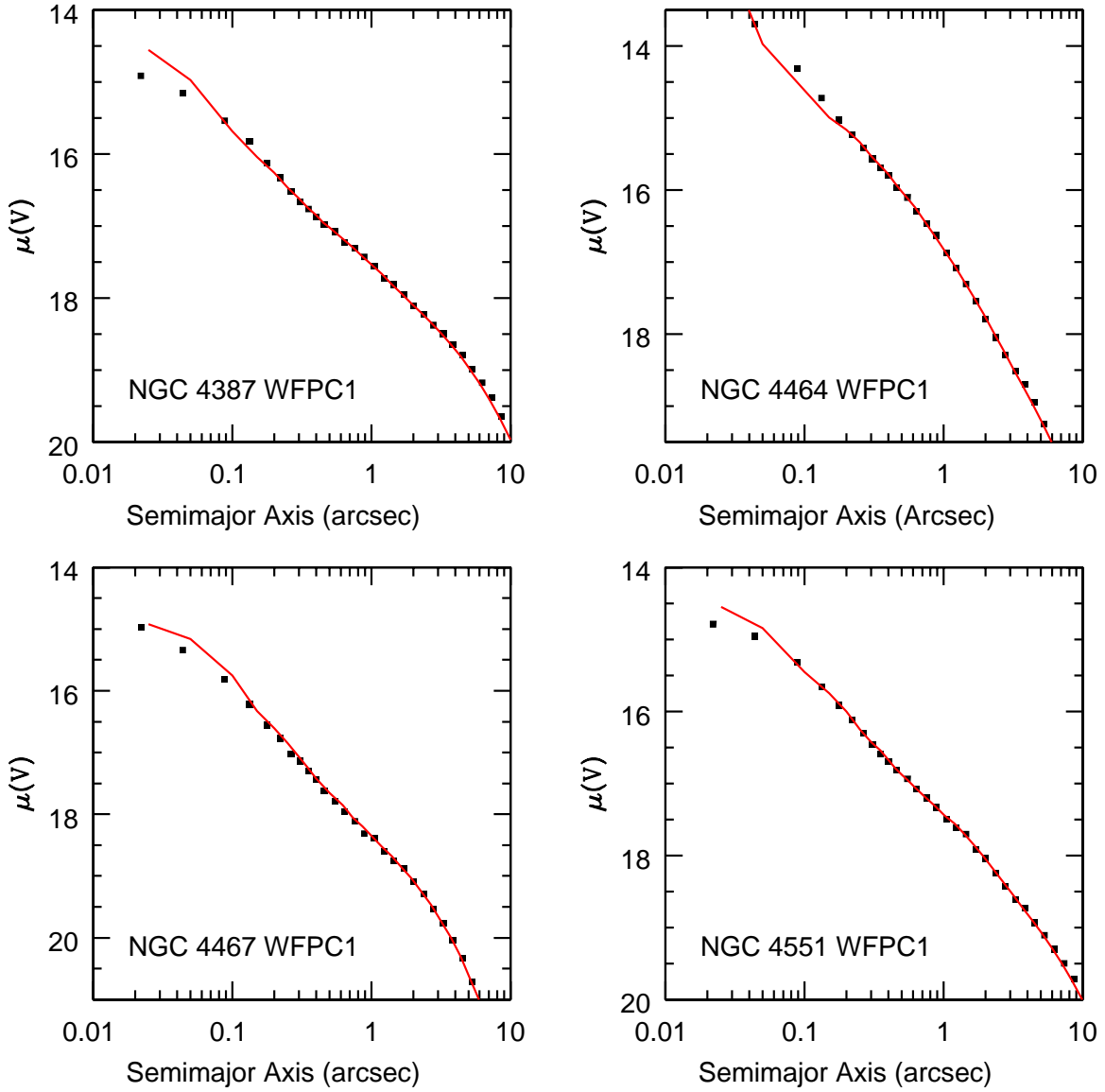
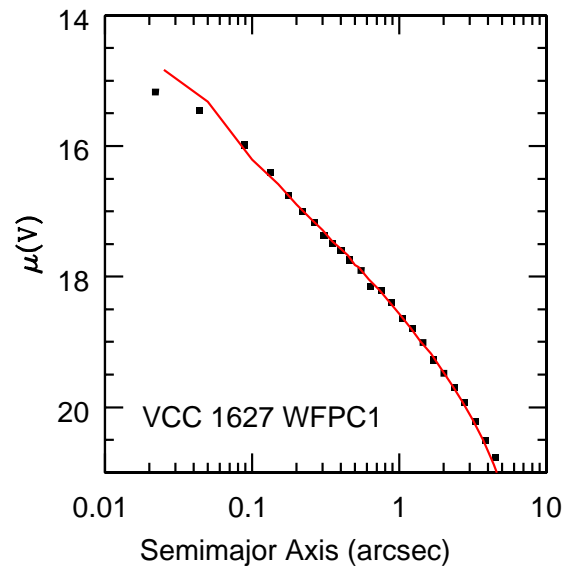
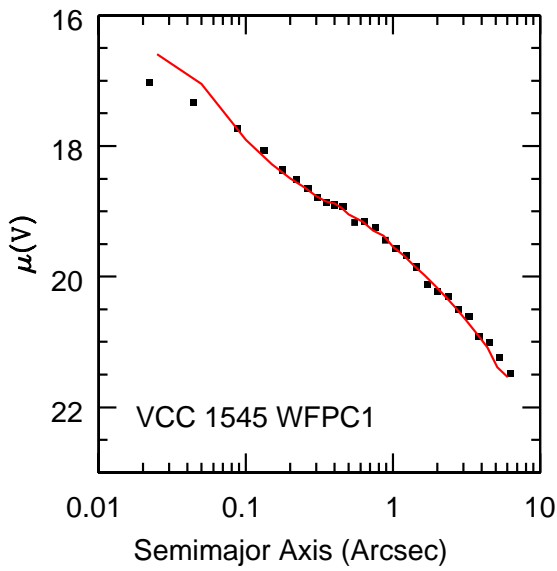
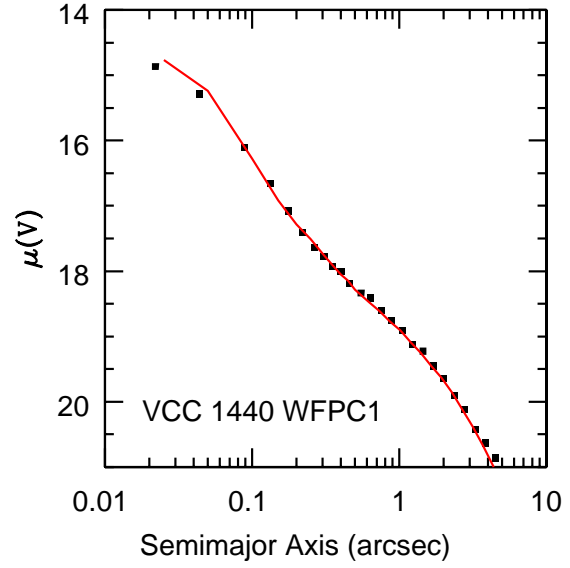
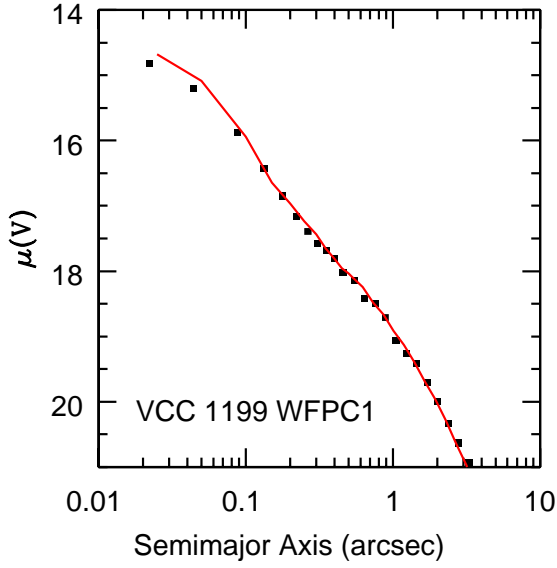
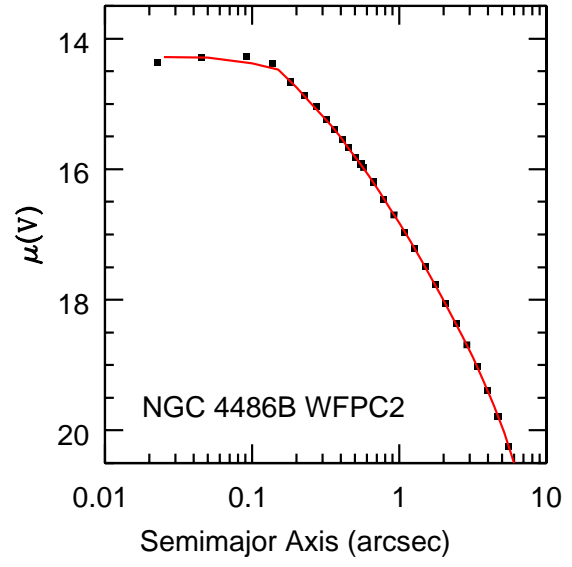
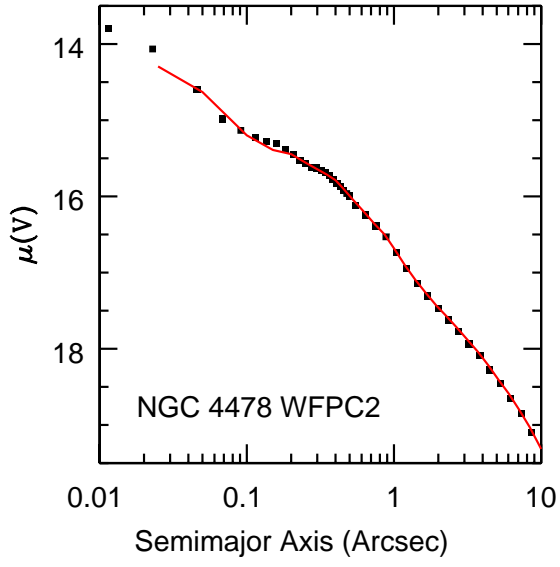


Fig. 10.— Deconvolved brightness profiles obtained with ACS/WFC are compared to WFPC1 or WFPC2 profiles for 10 galaxies in common to the present and Ferrarese et al. (2006) VCS sample. Profiles measured from the deconvolved and drizzled ACS/WFC F475W images are shown in red as compared to deconvolved F555W photometry from WFPC1 (Lauer et al. 1995) or WFPC2 (Lauer et al. 2005). The first eight galaxies were observed with WFPC1. NGC 4478 and 4486B were observed with WFPC2 (the NGC 4478 images were dithered to create an image with sub-sampled pixels). Deconvolved profiles from ACS, WFPC2, and WFPC1 images all agree well into $r \approx 0''.1$; interior to this radius the comparisons show that ACS/WFC has superior resolution to WFPC1, but that WFPC2 is superior to ACS.





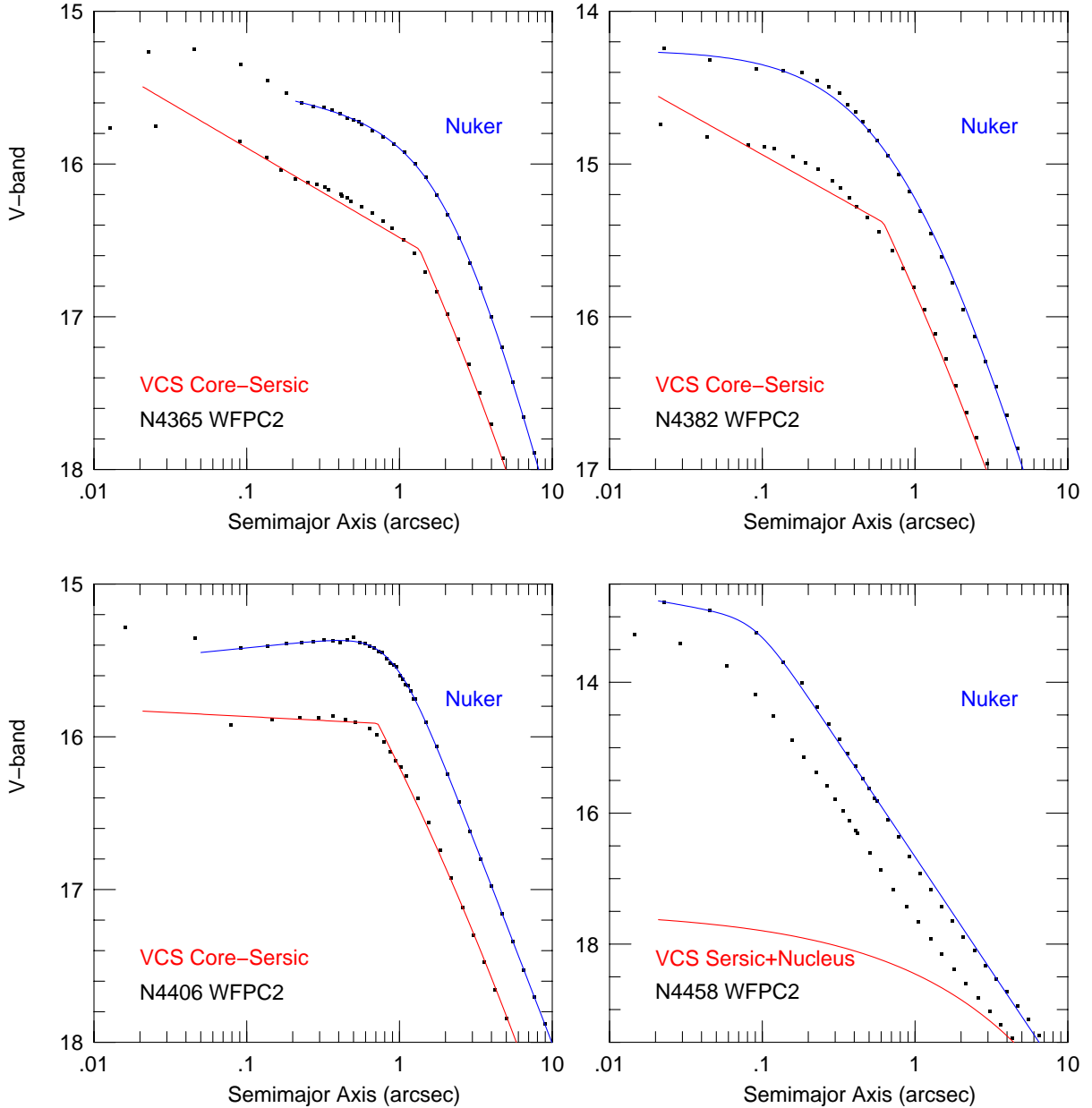
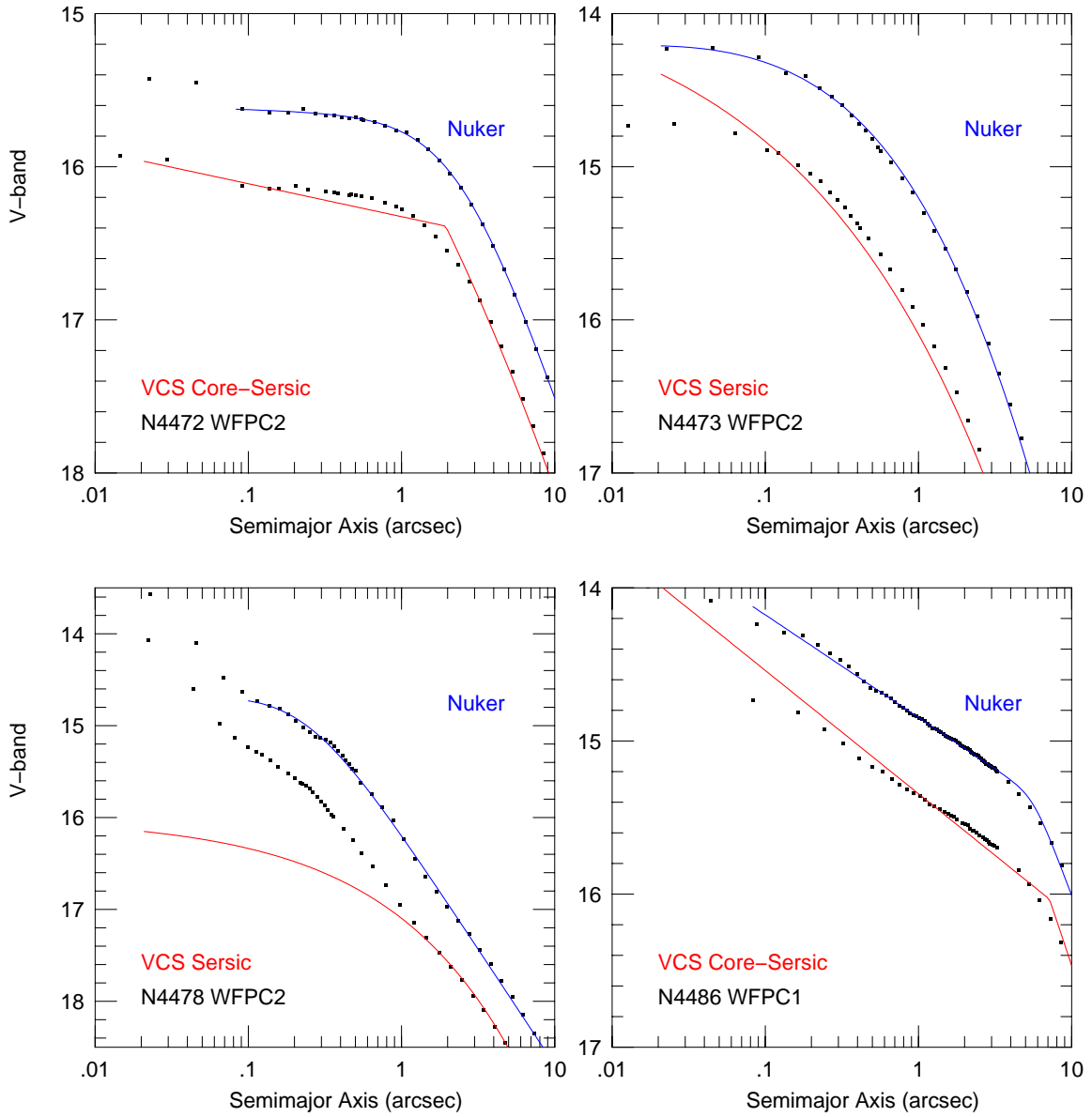
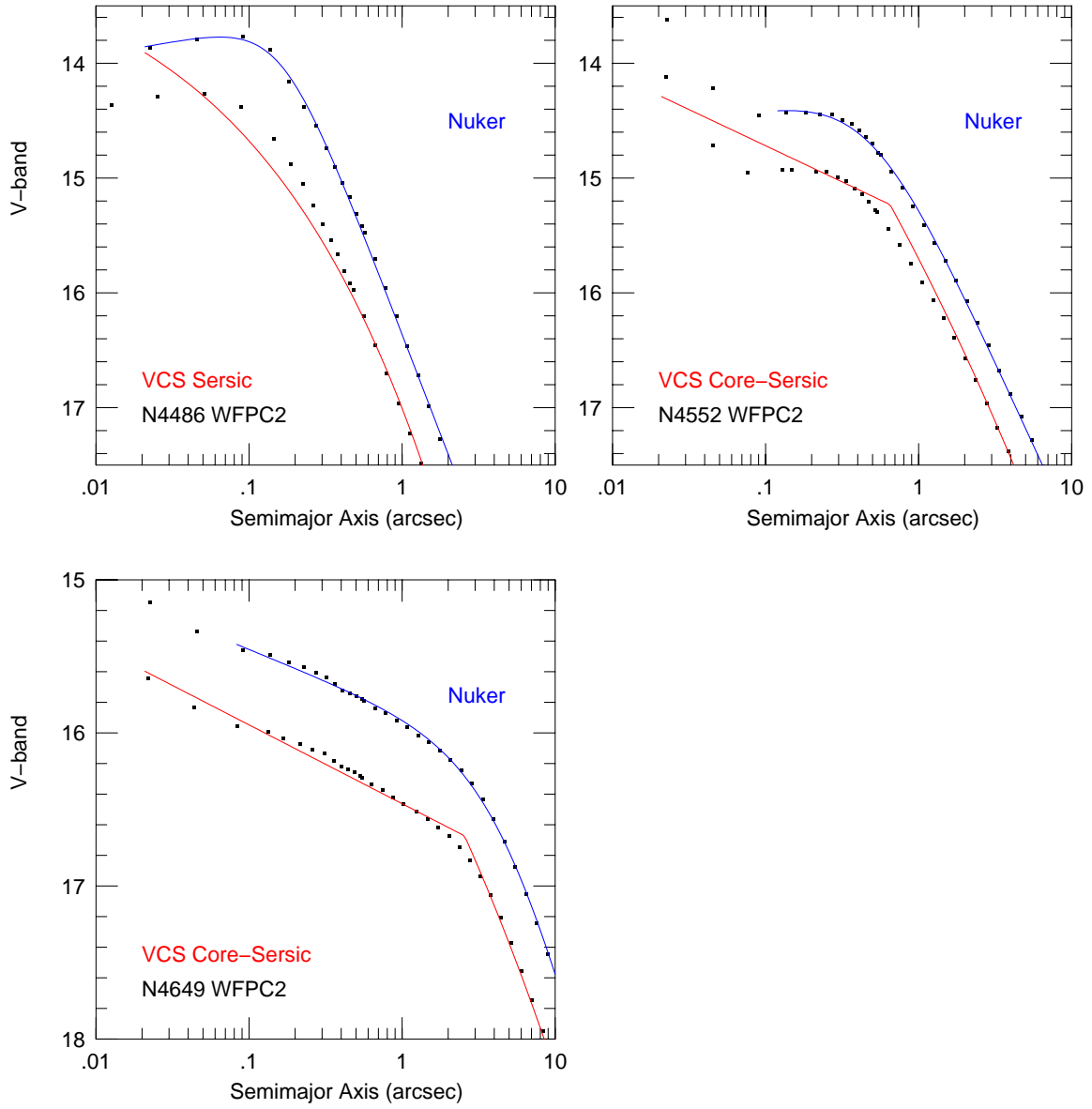


Fig. 11.— Nuker law fits (blue) are compared to the Ferrarese et al. (2006) model fits (red) for core galaxies in common between the present and VCS samples. The points are deconvolved isophotal surface brightness measurements obtained with WFPC2 (Lauer et al. 2005), with the exception of NGC 4486, for which WFPC1 was used (Lauer et al. 1992a). The photometry has been recast as a function of isophote mean-radius for comparison to the VCS models. The VCS models have been scaled vertically to account for the $g - V$ color difference by computing the mean offset between the data and models for $r > 2''$. The data used for comparison to the Nuker models has been offset by 0.5 mag for clarity. The legends in red indicate the type of the VCS model used, which is either a Core-Sérsic model, a pure Sérsic model, or a Sérsic model with an additional nuclear component. The nuclear components in the last model are not shown, however, as the Ferrarese et al. (2006) estimation of γ' is based solely on the Sérsic component.





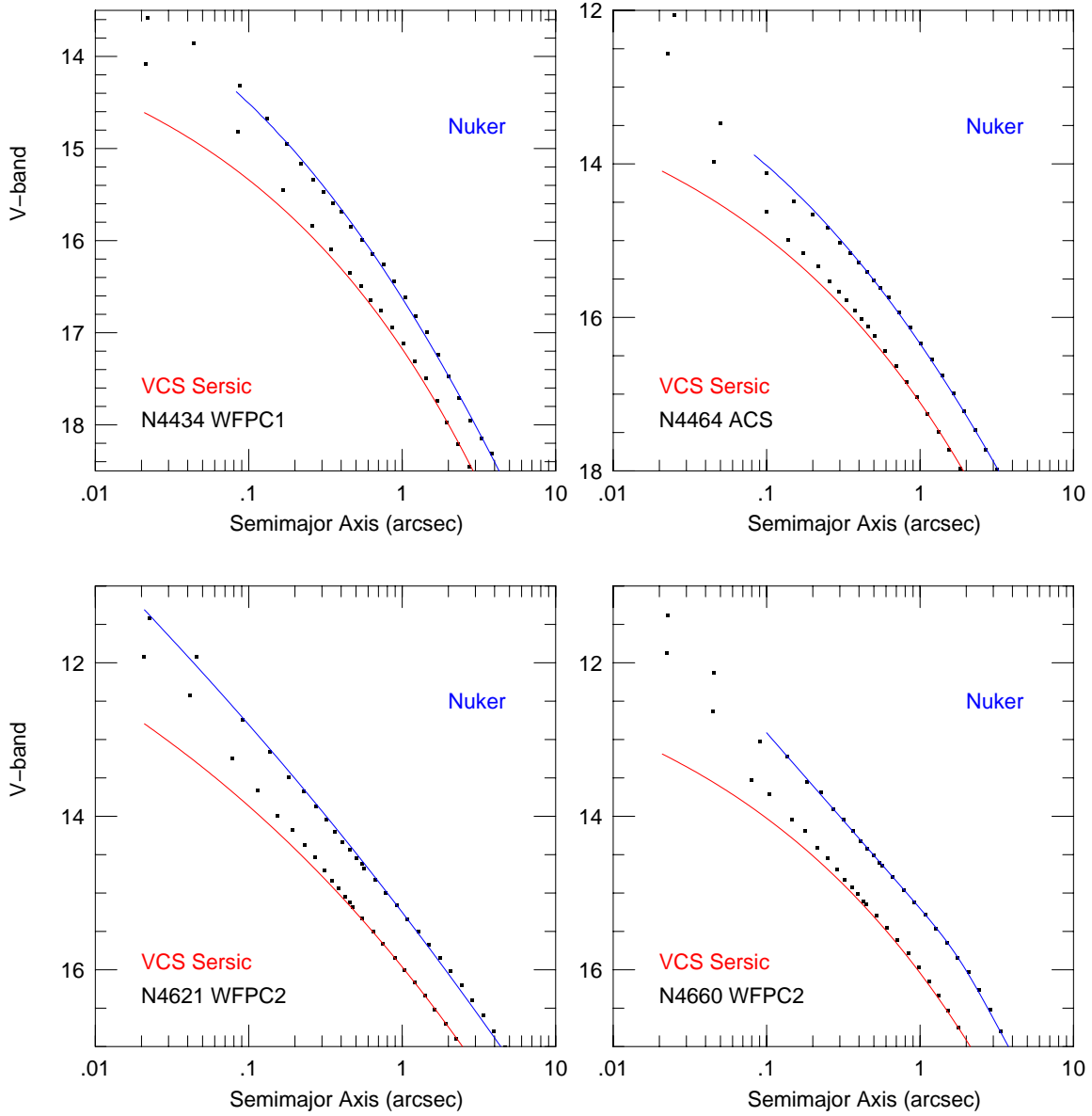


Fig. 12.— Nuker law fits (blue) are compared to the Ferrarese et al. (2006) model fits (red) for power-law galaxies in common between the present and VCS samples that Ferrarese et al. (2006) fitted with pure Sérsic models. The points are deconvolved isophotal surface brightness measurements obtained either with WFPC2 (Lauer et al. 2005) for NGC 4621 and 4660, or WFPC1 (Lauer et al. 1995) for NGC 4434, and ACS/WFC for NGC 4464. The photometry has been recast as a function of isophote mean-radius for comparison to the VCS models. The VCS models have been scaled vertically to account for the $g-V$ color difference by computing the mean offset between the data and models for $r > 2''$. The data used for comparison to the Nuker models has been offset by 0.5 mag for clarity.

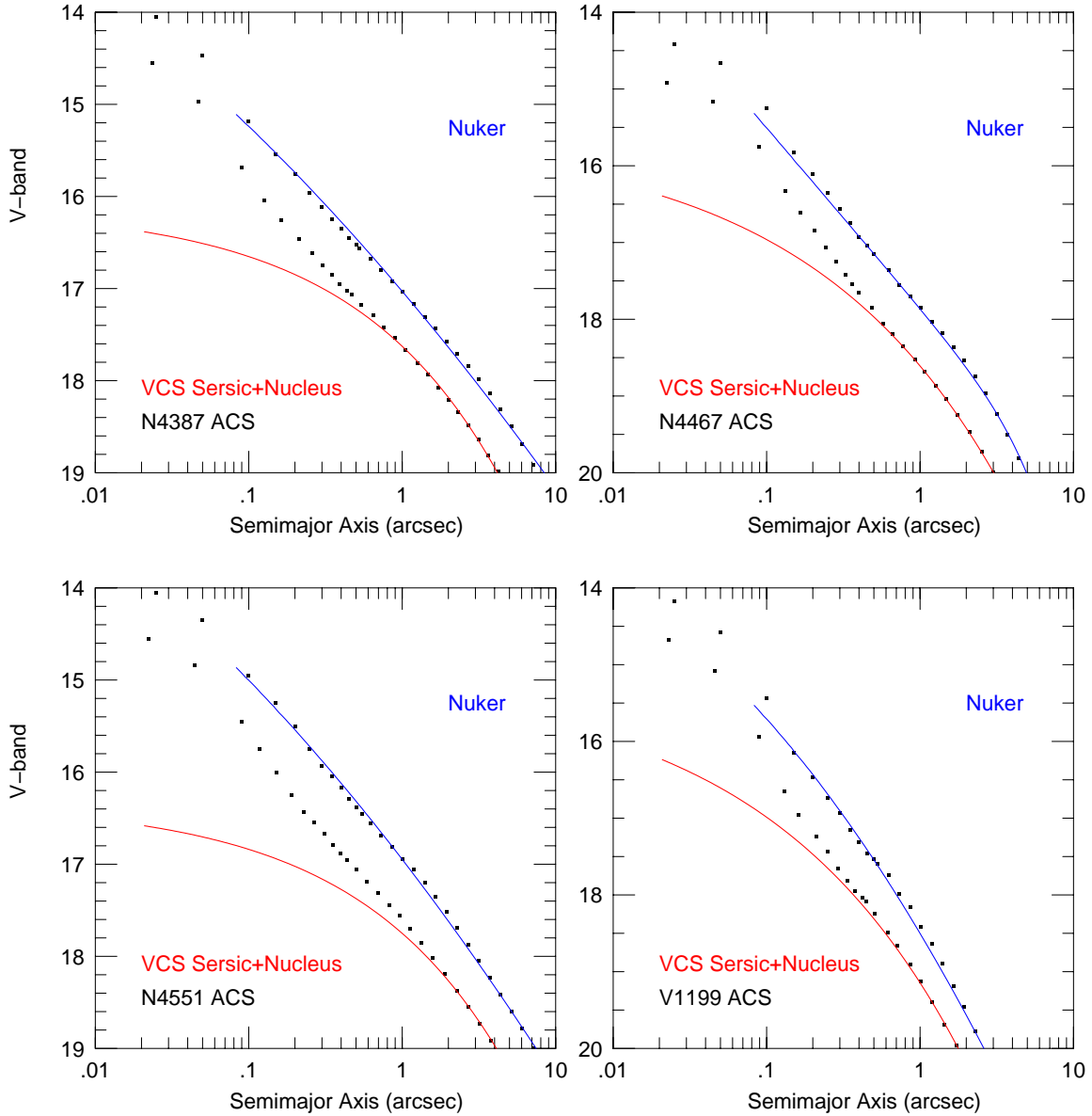
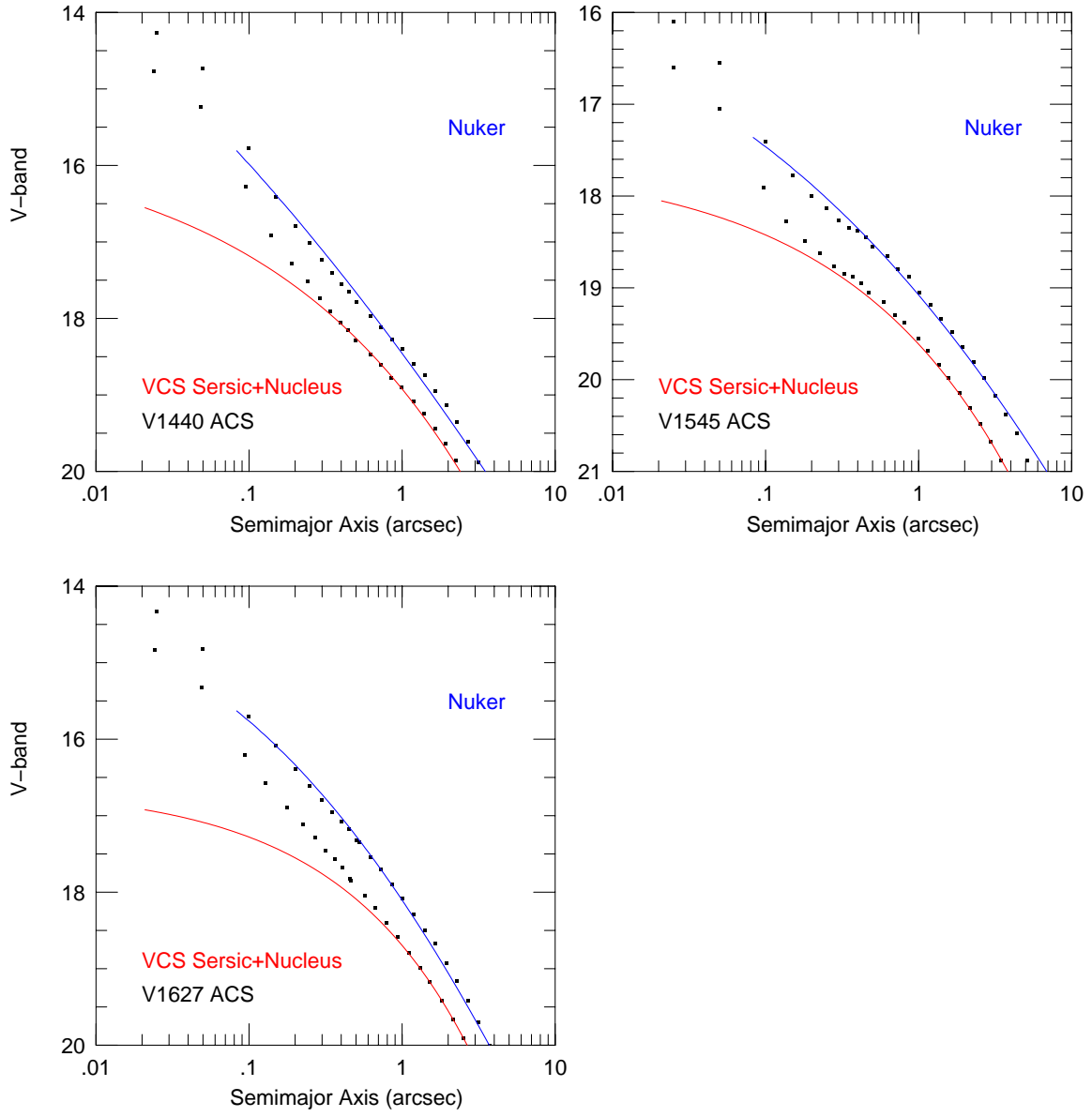


Fig. 13.— Nuker law fits (blue) are compared to the Ferrarese et al. (2006) model fits (red) for power-law galaxies in common between the present and VCS samples that Ferrarese et al. (2006) fitted with Sérsic + nucleus models. The points are deconvolved isophotal surface brightness measurements obtained from ACS/WFC images. The photometry has been recast as a function of isophote mean-radius for comparison to the VCS models. The VCS models have been scaled vertically to account for the $g - V$ color difference by computing the mean offset between the data and models for $r > 2''$. The data used for comparison to the Nuker models has been offset by 0.5 mag for clarity. The nucleus components fitted by Ferrarese et al. (2006) are not shown as their estimation of γ' is based solely on the models shown.



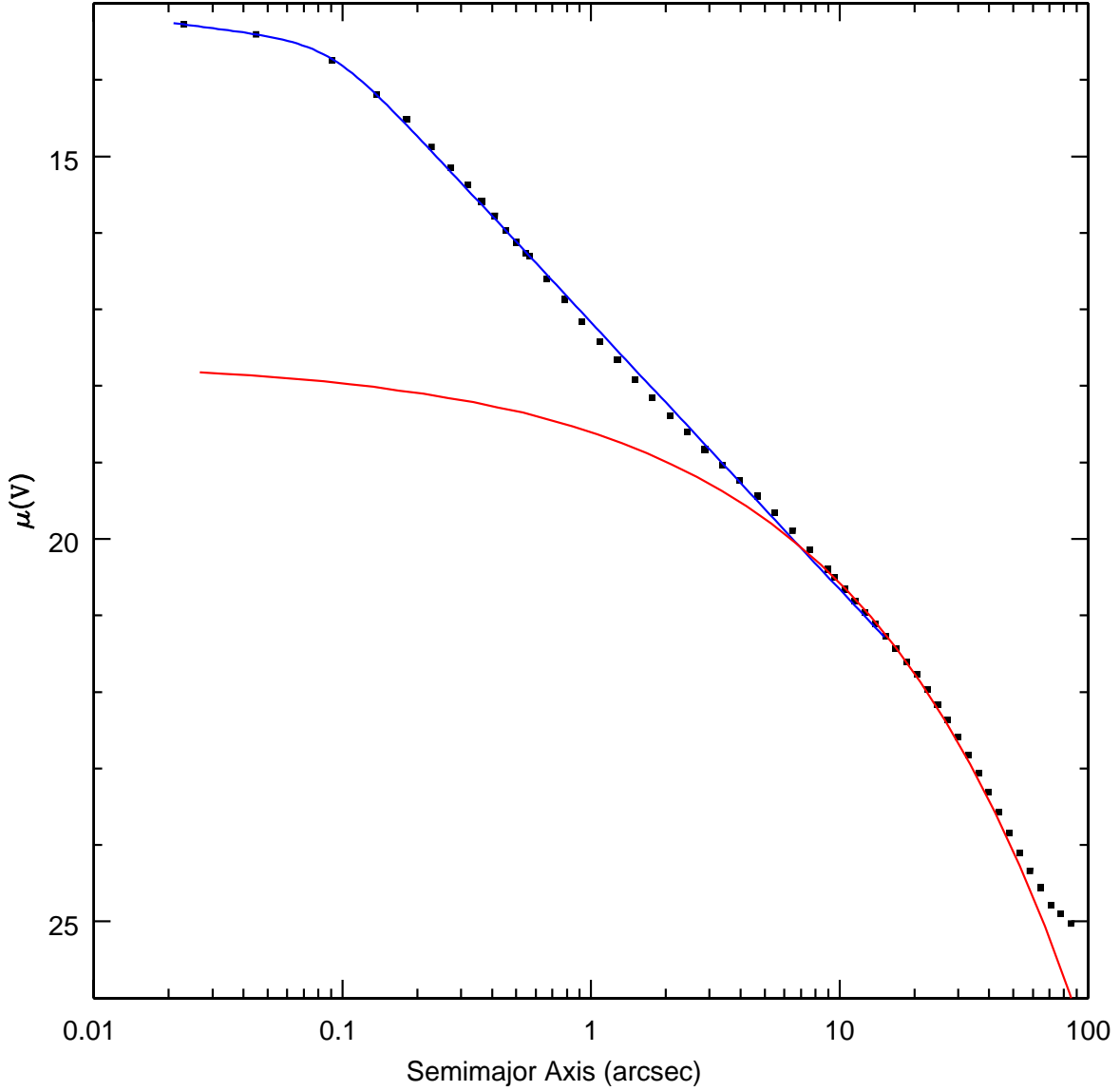


Fig. 14.— The VCS and present modeling procedures are compared for NGC 4458. The Lauer et al. (2005) deconvolved WFC2 V -band surface photometry of NGC 4458 extended to large radii by the addition of the Jedrzejewski (1987) B -band photometry for $r > 10''$ is plotted as black points. The Nuker law is fitted to NGC 4458 for $r < 15''$ and is plotted in blue, while the Ferrarese et al. (2006) Sérsic g -band component of their Sérsic + Nucleus model is plotted in red. The Nuker law describes the portion of the galaxy classified as a separate nuclear component in the VCS model, while the Sérsic component alone is used to estimate the VCS γ' value at $0''.1$. The Sérsic profile is adjusted from a geometric radius system to semimajor axis by the average isophote ellipticity at $r \sim 10$ ($\epsilon = 0.12$) and is scaled vertically assuming $g - V = 0.35$ mag.